General Remarks

We thank both referees for carefully reading the manuscript and providing clear and constructive comments for improving it. We highly appreciate their willingness to review a revised version of the manuscript. To our impression, most confusion and misunderstanding was caused by insufficient description, what should be addressed by our algorithm: the peak structuring. The simplifications made at prior (peak identification) and later steps (peak interpretation) were made to not distract from the major focus. This was not clearly communicated. We tried to be more comprehensible and precise in the formulation and included more material. The fundamental changes are briefly described here, before each point is addressed individually below. The referee comments are marked in grey and the response in black with indentation.

We revised the introduction and discussion section, to make the scope of this study clearer. More emphasis is put on the fact, that the novelty of our approach is the peak structuring part. The peak identification/finding and the interpretation step are kept rather straightforward on purpose. A second example Doppler spectrum was added to the algorithm description.

Both referees raised doubts about the quality of the dataset. We are confident, that the quality of the dataset is sufficient, especially when taking into account the conditions under which it was sampled (shipborne in the Arctic). However, we comprehend the problems that might arise from introducing a new method on an imperfect dataset. Hence, we decided to add a second application case study based on data from the ARM campaign BAECC at Hyytiälä, Finland.

We want to emphasize, that the algorithm itself is independent of the averaging time. We choose the 10 seconds average for the PS106 dataset for two reasons: Firstly, to smooth out the uncertainties arising from pointing uncertainties due to ship motions (especially after the breakdown of the stabilization platform). Fig 1. below illustrates this issue. Secondly, we wanted to be sure, that a detected local minimum in the spectral reflectivity is not caused by noise, i.e. reduce the number of false positives. One approach to reduce the uncertainty in the Doppler spectrum estimate is to sample more realizations and average [Zrnic 1975 JAM]. The standard deviation per spectral bin will reduce with $1/\sqrt{N}$. For our settings of 5kHz pulse repetition frequency, 256 FFT length and no coherent averages, the expected standard deviation per bin is 0.3 dB, which is sufficiently below the 1dB prominence threshold. Also work by other authors (as well dealing with KAZR data) had to do additional smoothing to get useful information from the Doppler spectrum. E.g. Luke and Kollias 2013 [JTECH] used a 20 second running window and Kalesse et al. 2019 [AMTD] used 18 seconds averages.

In the frame the averaging might hide few spurious features, but from our experience, the features we are interested in are persistent over times longer than the averaging time under such smooth and stratiform conditions as observed here.
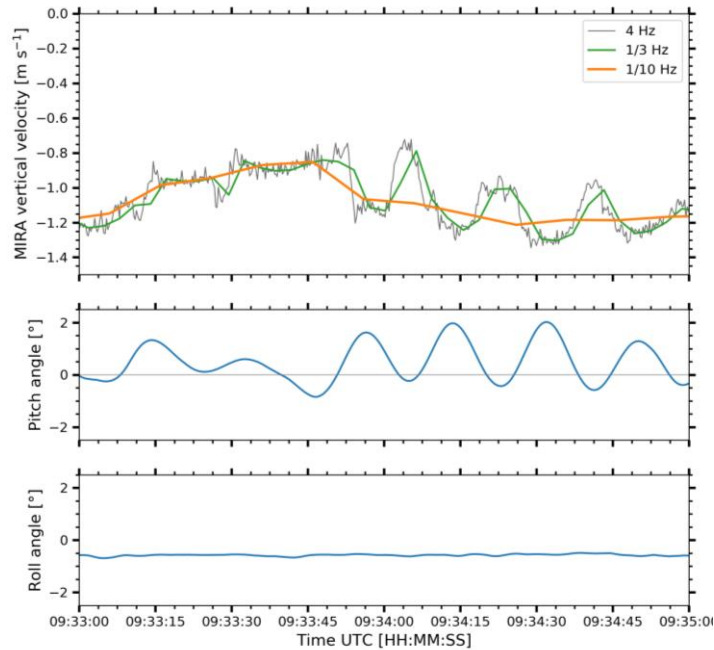
Fig 1 MIRA-35 vertical velocity in different temporal resolutions as well as pitch and roll angle measured by the ships navigation system

Specific Reply to Referee #1

A much more careful proof-reading by all authors is needed regarding the English, punctuation, typos, and sentence structure. I will list a few examples in the specific comments but not all. This should be one of the main duties of the co-authors rather than the reviewers.

> Thanks for this comment. We will consult a native English speaker before submission of the final version of the manuscript.

Algorithm description (Section 3): I recognize that the authors put a lot of effort in illustrating and explaining their new algorithm. However, I have to admit that I still got confused in some parts and would like to suggest a few improvements: In your example spectrum (Fig. 1) you show a spectrum with several sub-peaks but without an additional noise separated peak. I think such a more general example would be much better to illustrate the method. This would also better connect to your mixed-phase cases where one often finds the narrow, noise separated liquid peak next to the broader ice/snow peak with sometimes additional sub-peaks for example caused by riming. In such a diagram, I would also like to see all terms which are used in the text to be included. I was for example very much confused by all the node termination: root node, parent node, child node, leaf node, etc. Please make this easier for the reader to follow or to quickly figure out what is what.

> Thanks for the suggestion. We have added a sketch (new Fig. 1) to illustrate the indices and naming conventions.
> The figure illustrating the tree generation (new Figure 2) now contains two spectra. One including a noise floor separated peak and 9 nodes and the second one where spectral LDR is available.

I have my biggest problems with the second part of the case study (Section 4, P8, L5 and following). The description itself is very lengthy, descriptive, and contains a lot of speculations but very few clear conclusions. The fall streak analysis is also done very poorly by manually following streaks of maximum radar reflectivity. In that way, you are always tracking the largest particles which dominate the

reflectivity signal. There are many datasets (Cloudnet sites, ARM database) where you can do such an analysis in a proper way and at the same time take full use of your new mode identification: Simply take the horizontal wind profile and the mean Doppler velocity of your nodes and you can reconstruct the fall streaks of your individual nodes. The current fall streak analysis you present appears to me not very convincing.

> We now emphasize more clearly in the text that we used a simplified fallstreak tracking procedure. References to more sophisticated methods are given in the text (now: P12, L3-15). However, we also need to note here that the fallstreak tracking based on the horizontal wind profiles works only in case of absence of directional wind shear. In the presented case, the wind direction in the height range covered by the tracked fallstreaks varied between from 230° to 300° and back to 150° (Fig. 2 below).
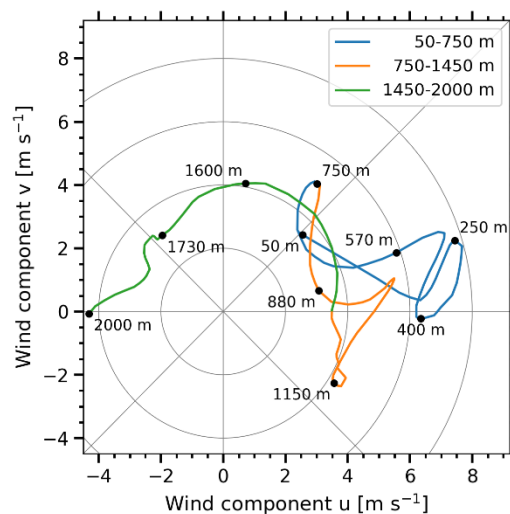
Fig 2: Hodograph from the sounding shown in the manuscript (29 June 2017 10:50 UTC).

Also the application of the Hogan 2006 Z-T-IWC retrieval to the different nodes is not very sound. As you mention, Hogan et al., 2006 derived the Z-T-IWC for a large set of aircraft measured PSDs. I find it very questionable to apply such a relation to your different nodes, which you identified in order to separate (!) different particle populations and their different properties. You could have used (or even self-derived) Z-IWC retrievals for more column or needle shaped particles (for your mode with larger LDR at lower levels) and a Z-IWC retrieval for aggregates or plates for the first mode. In that way you would have demonstrated some convincing added value of your peak separating approach. I suggest to either shorten/remove some of these parts or extend it (better datasets, other cases, more appropriate Z-IWC relations).

> We agree that the Hogan 2006 retrieval is not optimal here, because it is designed for a single particle species (aggregates) and the underlying dataset was derived in deep clouds. In Cloudnet, for which the Hogan 2006 retrieval was originally designed, the retrieval is usually applied to all clouds, independent of their nature. In our case, we see the precipitation from two stratiform clouds overlapping. Hence, the principle application is nearly the same as usual, taking into account the error intervals for the temperature range given in Hogan et al. (2006). In the context of this paper, the IWC values are presented to give an impression on how the mass relation is between the single peaks. This is actually only possible if peaks were successfully separated first. Nevertheless, we decided to modify Fig 9 (former Fig. 6) in such a way that it now presents the total IWC (node 0) and the ratio of the IWC of the selected node to the total IWC. This should give a better impression of the applicability of peakTree for the

investigation of the microphysics of different nodes. For future work, we would like to use other retrievals based on the actual shape of the particles.

I am also missing some discussion in your manuscript about how to best decompose Doppler spectra. Several studies in your reference list used for example Gaussian fitting or fuzzy logic while in your approach you basically cut the spectrum at the minima. I understand that your focus in this work is in the peak identification logic but I would welcome some discussion on this topic as well since it appears to me to be closely connected.

> We would consider the focus of the algorithm to be on peak structuring. From our point of view, the peak decomposition step should be called peak identification.

> However, the performance of the fuzzy logic, continuous wavelet transform or fitting techniques are more powerful, if the peaks that are noise-floor or local-minimum separated are segregated beforehand. Then these techniques could focus on identifying hidden sub-peaks in a mono-modal appearing peak.

> We rewrote the respective section in the introduction to make this issue clearer.

Abstract, L. 2: "Cloud radar observations contain information on multiple particle species, when there are distinct peaks in the Doppler spectrum". This is not always true. Turbulence can cause multi-modal spectra even though only one population of particles is present.

> Thank you for pointing this out. We weakened the statement by including 'frequently'.

Abstract, L. 3: "Complex multi-peaked situations are not captured by established algorithms". Not clear to me what you mean here. What means "complex"? What is "not captured"? What should be captured and for what? Be more specific.

> 'Complex' is omitted, as it is implicitly included into the 'multi-peak' statement. 'not captured' was replaced by 'not taken into account'.

P2-3, Dataset description: It appears to me that the dataset is not really ideal for demonstrating the algorithm for Doppler spectra analysis. 10s averaging will remove a large number of interesting microphysical features and also the horizontal wind influence due to pointing uncertainties can cause many artefacts. I understand that you probably want to use data of recent campaigns to acknowledge these projects and their funding but from a scientific point of view it appears to me that there are several datasets (e.g., ARM datasets from the Arctic) which provide much better quality for such a demonstration.

> As both referees raised this concern, we discussed it above in the General remarks section.

Figure 1: Why does the spectrum have these "tails" to the sides (lowest/fastest velocities). It looks like a broadening effect due to the long temporal averaging and/or swinging of the beam with the ship motion.

> We are puzzled by these tails as well. So far we could exclude effects from averaging, ship movement and FFT windowing. Currently we are in contact with the manufacturer, who presumes a rather low level technical issue.

P3, L12: "with signal above the noise level": Please provide the exact threshold when you consider the signal to be above the noise.

> We cannot provide one threshold, as noise also depends also on range. Nevertheless, we refined the mentioned sentence: 'Hence, when calculating the LDR (Eq. A6) only bins where the signals in the cross channel is a factor of 3 above the noise level are taken into account.'

P3, L20: I can't find v_left/right/add in Fig. 1. Are they not relevant for the algorithm? As I mentioned in my general comments, it would be good to show an example, which contains a noise-separated peak. Here, you only describe it but in such an example, you could easily explain all terms used.

> We added a noise-floor separated spectrum and the descriptions into the figure, which is now Fig. 2.

Figure 1a: I suggest to remove the "units" of the spectral reflectivity (dBZ) and rather use arbitrary units [a. u.] or [dB]. If you would plot the spectrum in linear units, you could write (mm^6/m^3)/(m/s). In that way, the integral over the full spectrum would result in the usual linear units of Ze. However, the integral over a log spectrum will neither result in mm^6/m^3 nor dBZ. The radar experienced readers will certainly understand what you mean but it's simply not correct in a strict scientific sense.

> Thanks for pointing to this issue. We settled to [a.u.] (now in new Figure 2)

Figure 1b: It is not clear to me how I can read the skewness from the triangle, please explain. The caption is also missing the description of what is meant with "spec Z cx" or the line "decoupling".

> The triangle is only a qualitative indication for skewness, we included a clarification as well as a description of the mentioned terms to the caption (now Figure 2).

P3, L32-33: "Only the part of the Doppler spectrum above the threshold defined by the spectral reflectivity minimum that separated the peaks are used". This is a problematic aspect of your approach which I think should be discussed much more and maybe even changed. Let's consider only Ze: For Node 0 you integrate the full spectrum starting at the noise level. Already for Node 1, you integrate only starting from your first threshold (-34 dB). I don't understand why you are not integrating again from the noise level? I would expect that when I sum up all the identified sub-peaks (Node4+3+2; I exclude Node 1 since it is basically 3+4), the resulting Ze should be identical to Node 0. But if I understand correctly, this is not the case for your algorithm, or? From a microphysical point of view, I guess one would like to have moment estimates of the full sub-peak and not only the "peak head" which sticks out of the remaining spectrum.

> Thanks for pointing out this ambiguous formulation. The comment addresses, what we tried to explain in the Appendix with 'To prevent this, only spectral reflectivity values S(i) above the threshold that separates the subpeak from its neighbor are included for calculating moment other than Z.'
> We added Fig A1 to illustrate, why it would introduce a bias in higher order moments, when integrating over the whole peak (-0.37 vs 0.09 for the left peak). However, for the reflectivity, the concerns are valid. The revised explanation reads: 'Reflectivity Z is calculated by integrating the spectral reflectivity of the whole peak (i.e. from the noise floor up). For all higher moments, signal below the threshold, that separated the (sub-)peak is neglected to avoid biases (see also Fig. A1)'

P4, L3-4: Where do I find Node 5 and 6 in Fig. 1?

> Nodes 5 and 6 would exist if node 2 (the rightmost sub-peak) would have two sub-peaks. We have added a sketch (new Fig. 1) with possible indices in the beginning of the algorithm description.

P6, Title Section 4: Replace "ice crystal habits" with "ice crystal populations". The spectra indicate that you have two populations of particles with different fall velocities. This could be related to different habits but you could also have two populations with different fall speed and similar habits (e.g. due to onset of riming).

> Done as suggested (P9,L19).

P6, L9: "humidity profile": Actually you only show profiles of air temperature and dew point. The humidity information is contained in them but why not plotting relative humidity directly?

> We replaced the term 'humidity profile' by 'spread between temperature and dewpoint' (P9,L25). However, we decided to stick to dewpoint and temperature as plotted variables (now Fig. 6). Firstly, dewpoint is a more direct measure for moisture content, as relative humidity depends strongly on air temperature. Secondly, relative humidity would have required a new subfigure or at least new x-axis, which would make the plot more difficult to read.

P7, L2-3: "previous studies used the simple criterion of low reflectivity and vertical velocity close to $0 ms^{-1}$ to identify regions of a cloud, where the presence of liquid is likely" I think this description is not very precise: In fact, the peak is thought to be due to liquid if it is a very narrow peak since the PSD of super-cooled droplets can be assumed to be rather narrow. In the way you describe it, any peak with low Ze and v close to 0 m/s might be interpreted as liquid. How reliable are those thresholds (especially the Ze threshold)? Are your values different from the studies cited? Are the thresholds used within those studies all the same or different?

> We use the same thresholds as Oue 2018. Kalesse 2016 also reported similar values. Yu 2014 and Frisch 1995 used slightly higher reflectivity thresholds. Our choice of -20dBZ is rather conservative compared to these studies. Judging, how reliable the threshold are is beyond the scale of this study. However, the good agreement with the ceilometer cloud base, especially in the BAECC case makes us quite confident.

Figure 3f (new Fig. 6f): Why is there no color for N=2? A second node would be the most likely scenario for a liquid water and an ice peak, or?

> A full binary tree with two nodes is not possible. Either, the tree contains only the root node (mono-modal spectrum) or left and right sub-peak, hence 3 nodes in total. I.e. the situation of ice and liquid water peak will be N=3.

P8, L1+6: Be consistent whether you use the minus sign when indicating the Doppler velocity or not.

> Done as suggested.

P8, L1: The low LDR indicates plate-like particles, right? But then they are oblate and not prolate (like columns). At P12, L11 you denote them as oblate.

> 'oblate' is the correct term in this context. Thanks for mentioning.

P9, L24: "indicating no change in particle habit": Well, if the particle habit changes for example from plates to dendrites, I would also not expect a big change in LDR. I think the conclusion that habit does not change only because LDR is rather constant is not true in general.

> The argument of the referee is perfectly right for the general case. For this specific case LDR values of -14dB can only be caused by strongly prolate particles (like columnar ice needles). Any change towards more oblate particles due to aggregation or riming would decrease LDR. We modified the statement, to make this special case clearer (P13,L5): "During this growth, LDR remains at the high value -14 dB, indicating no change of the prolate particle shape."

P9: In addition to my principal problems with your fall streak analysis (see general comments): Why don't you show range spectrograms for your different fall streaks?

> We decided to not show the spectrograms because this would have increased the amount of Figures without providing additional information. To our notion, the general nature of a

spectrogram is already depicted in the moment plots of the two main nodes in Fig 8 (formerly Fig. 6).

P12, L4: Another important advantage of your method to microARSCL is that you provide the code for the community. For further development of Doppler spectra analysis, this is absolutely key!

Thanks for emphasizing this.

P13, L7: Why are v_left/right relevant for the moment estimation. They don't appear in any formulas. How are they actually determined? Maybe a certain threshold for the spectrum above the noise level?

v_left and v_right appear in the formuals implicitly via the summation indices i=l to r. The relation between v_left and l as well v_right and r are described in the paragraph above.

Abstract, L. 3: Add comma after "In this study" and before "that". These are very typical punctuation mistakes, which I found very often throughout the manuscript. I will not list hem all but ask all authors to do a more careful reading.

Thanks for the hint. We corrected the error.

P1, L15: Better: "Cloud radars are frequently used.." P1, L17: Add comma after "In general" P2, L.4: Add comma "formed ice, and" P2, L7: "In a further step," P2, L7-9: Confusing and very complicated sentence. Please re-structure and/or split in two. P2, L10: Prior approached should be approaches P2, L12: Remove comma after "available" P2, L14: "In this study," P2, L16: "algorithm IS easily applicable" P2, L24: More a question to the editors but are citations of manuscripts in preparation appropriate? P3, L20, L31: "In a first step," "In the next step," P3, L23: Add comma after v_add P3, L22: Better "All minima found" P7, L1: Remove comma before "that" P7, L2 and P9, L3: "can not" vs "cannot" use consistently P7, L7: "during the whole case study" better "during the entire event" P7, L7/L8: "The top/second one" is a bit slang-like, better "The uppermost layer" P7, L7: "single moments of the full spectrum": I think the "single" is redundant here P7, L9-10: "Together with the lidar backscatter indicating a liquid cloud base at 750m between" awkward sentence, please rephrase. P9, L4-7: Very long and complicated sentence. Split in two and rephrase. Also, the sentence is very speculative. P9, L1: add comma before "which" P12, L6: application OF this new P12, L6: In a second step, P12, L13: Within this liquid layer,

Corrected all mentioned errors. Thanks a lot for the effort!

Specific Reply to Referee #2

Impact of 10s averaging: 10s is quite a lot for spectral cloud radar applications. Most cloud radar data set I'm aware of (e.g. ARM) use temporal resolutions in the order of 1-3 s. What is the impact of this on the method? I would expect that the spectrum is bumpier when averaging less and that maybe a different sub-peak threshold needs to be used?

The generation of the tree itself is independent of the averaging time. However, a noisier 'bumpier' spectrum would cause numerous narrow nodes, which would increase the effort necessary for post processing, especially peak interpretation.

At the same time, sub-peaks might get smoothed out during averaging. And do I assume correctly that the authors hope that the ship motion cancels out within 10s?

As both referees raised this concern, we discussed it above in the General remarks section.

Using Doppler spectrum above the separation threshold for moment estimation: I think I understand why the authors decided to estimate the moments this way. However, I'm afraid that this method will

also lead to biases, in particular for the higher moments. The authors could do a quick sensitivity study and quantify the change of the moments by using a normal monomodal peak and cutting of the tails at different spectral reflectivities.

> Currently, we separate the peaks above their floor to get rid of basic systematic errors introduced into the calculation of the skewness when considering a peak which is cut off at one or both sides. To our knowledge no better approach to deal with such situations is available yet. The skewness measured above the threshold can only be compared to the original skewness in a very limited way and must be treated with caution. It will probably have the same sign, but the magnitude will be different, because the numeric value of skewness reacts very sensitively to changes in the outer parts of a peak. We mention this now in the paper in Section 3.1 and in Appendix 1.

Grouping: The authors should discuss why they chose the threshold used for the grouping (50s, 150 m, d<0.9, 0.4 and 0.9 normalization factors) and the impact of changing these thresholds on the results. Application of grouping: I would strongly recommend adding a few sentences on how the data set was grouped exactly. I do not understand a couple of processing steps: Did the authors manually select anchor nodes for both nodes separately? What criteria were used?

> We admit, that the choice of the thresholds seems arbitrary on the first look. They are the result of manual and iterative interpretation. The quality criterion for the grouping is the consistency and smoothness of the moments in time and range for each particle population. A new paragraph in the 'Discussions and conclusions' section discusses the impact of each threshold. We want to emphasize again, that this grouping approach is no prerequisite of the peak structuring algorithm, but an example how this structure can be used to interpret peaks.

Were the criteria for liquid nodes used in Fig 4 used as a starting point for one node?

> The criteria for the liquid nodes were not used for this interpretation. But during the data analysis itself, the two detected liquid layers triggered a more thorough investigation of this feature.

What about other nodes then the two shown ones? Can they be grouped, too?

> In principle, they could be grouped, too. This second grouping step would only provide additional information for trees with more than 3 nodes. Also for the BAECC case grouping might be an interesting analysis, but is beyond of the scope of this study.

Language: The paper needs a lot of work to improve the English. German grammatical structure shows through in numerous places. Word selection and punctuation can also be improved upon. Given that publishing includes language editing for Copernicus, I do not list language-related issues.

P1L19: I would recommend adding a short discussion about the difference between peaks that are separated by noise and peaks which are not (eg see fig 13 of Williams et al 2018)

> From our point of view, there is no conceptual difference between noise-floor separated peaks and peaks only distinguishable by a minimum in spectral reflectivity. We added a paragraph on this issue in the discussion (P16,L1-7).

P2L2 "which likely causes significant errors": Are the authors sure? I would argue that for most empirical retrievals the climatology of multi-peak situations is (unknowingly) included into the retrieval so that there are no biases. Also applies to P9L30.

We here provide a reply that we also gave to a similar comment of Referee 1: In the context of this paper, the IWC values are presented to give an impression on how the mass relation is between the single peaks. This is actually only possible if peaks were successfully separated first. Nevertheless, we decided to modify Fig 9 (former Fig. 6) in such a way that it now presents the total IWC (node 0) and the ratio of the IWC of the selected node to the total IWC. This should give a better impression of the applicability of peakTree for the investigation of the microphysics of different nodes. For future work, we would like to use other retrievals based on the actual shape of the particles.

P2L23: I don't think the authors can cite papers in preparation

The paper will be submitted by the end of the review process. Basically the paper of Griesche et al. is a considerable extension in comparison to the information about the instruments given in Wendisch et al. (2018).

P2L29: vertical-stare -> vertically pointing

changed

P2L30: This part could be shortened using a table with the radar specifications.

A new Table 1 with the radar specifications (now for both radars) was added.

P3L12: LDR -> LDR spectrum?

Here the 'bulk' LDR is meant. The LDR spectrum is not used at all, only the co and cross channel spectrum.

P3L28f "the prominence of one of its subpeaks is less than 1 dB" and "height of the peak above": I assume the authors talk about the maximum of the subpeak?

Thanks for pointing out that sloppy formulation. We have refined the paragraph (P5,L6 and further): 'A minimum is skipped, if the prominence of either of its subpeaks is less than 1dB. Prominence is the difference between the maximum spectral reflectivity of a subpeak and the threshold that is defined as by the spectral reflectivity at local minimum (dashed grey lines in Fig 2 (a); similar to Shupe et al., 2004).'

P3L32 "Doppler spectrum above the threshold": In the appendix, the authors mention this does not apply to Ze?

Referee 1 addressed this ambiguous explanation as well. We added Fig A1 to the Appendix in order to illustrate why it would introduce a bias in higher order moments, when integrating over the whole peak (-0.37 vs 0.09 for the left peak). However, for the reflectivity, the given concerns are valid. The revised explanation reads (P5,L10f): 'Reflectivity factor Z is calculated by integrating the spectral reflectivity of the whole peak (i.e. from the noise floor up). For all higher moments, signal below the threshold, that separated the (sub-)peak is neglected to avoid biases (see also Fig. A1)'

P4 Fig1a: According to P3L19f, node 0 is the full radar Doppler spectrum

More clearly, it is the full Doppler spectrum above the Hildebrand Sekhon noise threshold. We refined the formulation in the text. We have rephrased the algorithm description, the mentioned sentence now reads (P4,L15-16): "The root node contains all signal of Doppler spectrum above the noise threshold between -v_Nyq and +v_Nyq." The Nyquist velocities v_Nyq of the involved cloud radars are given in Tab. 1.

P4 Fig1b: An explanation of how skewness is actually displayed in the figure is missing.

Thanks for pointing to that issue. We modified the figure caption (now Fig. 2) accordingly. 'Spectral width and skewness are shown by grey lines and triangles, respectively' now reads 'Spectral width is indicated quantitatively by the length of the grey lines and sign of the skewness is indicated by a triangle (pointing to left for negative skewness and vice-versa).'

P4L1: node 0 -> node 1?

No, node 0 (or the root node) is correct in this context.

P5 Table1: Z is not defined yet. Also, I strongly recommend to use Ze (equivalent radar reflectivity factor) instead of Z (radar reflectivity factor) because Z is typically defined with $10*log10(SUM(N*D^6))$ which applies only to Rayleigh scattering of liquid drops (see eg. 'Radar for Meteorologists' by R. Rinehart.

Thanks for addressing this point. The equivalent radar reflectivity was already used implicitly. We added a sentence in Appendix 1 to clarify.

P5L1: I would recommend indicating that 'indices' refers to the nodes not the bin in the Doppler spectrum.

Thanks for the suggestion, the column title now is 'Node index'.

P6 Fig2: Are Ze and v normalized in this plot?

No, the plot (now in Fig. 3) shows the actual values. Only for calculating the Eucledian distance d, the normalization described in the text is used.

P6L14: 'giving hints' please specify

We added ", such as size or shape." to the end of the sentence (P9,L31).

P7 Fig3: I would recommend adding the fallstreaks also to this figure because it is interesting that the lower end of the first one can be only seen after applying the grouping.

The fallstreaks were added to this figure (now Fig. 6).

P7L3 "to identify regions of a cloud, where the presence of liquid is likely": I would say these thresholds are rather to identify regions where drops are the dominating particle type. Liquid is likely also present in other cloud regions.

Thanks for mentioning. We moved this paragraph to a dedicated subsection (3.2.1) in 'Algorithm' section and rephrased it. However, the drops are not required to be the dominating particle type, they only need to cause their own (sub-)peak.

P7L9 "periods of liquid" add 'likely' or 'possible'

Done as suggested.

P7L9f: The liquid extends from 750 to 1000 m?

Most likely, as there is also a layer of high humidity indicated by the temperature/dewpoint profile from the sounding at these heights (see Fig. 6).

P7L13 "The faster-falling particle population" and title Fig 5: was velocity or LDR used or grouping? Also, I would recommend naming the nodes consistently.

For the manual assignment of the anchor nodes reflectivity, velocity and LDR was taken into account. The automated grouping only used velocity and reflectivity.

P7L15 "generated ice": the authors should mention before that they assume the second peak to be ice

> This sentence refers to the ice formed at cloud top, where no second peak is present. We modified the sentence to make this clearer (P11,L4f): 'Below 2.5 km height, the ice particles generated at cloud top descent with velocities of […]'

P8 Fig 4: Because it is described in the section before, I would recommend to clearly indicate that the grouping is not used in this figure.

> Indeed, this was confusing in the original manuscript. We moved the description of the liquid node selection and the grouping into separate subsections of the Algorithm section and referred to the respective subsection in the caption of now Figure 7 (former Fig. 4).

P8 Fig 4: I would recommend indicating the ceilometer cloud base by e.g. a black in this and other plots

> Thanks for the suggestion. We added the cloud bases for both case studies (now Figures 4, 5, 6, 7 and 8).

P8 Fig 4: How does LDR look? It should have a sufficient SNR at least for the lower layer.

> The referee raises an interesting question. LDR for the liquid peak is shown in Fig. 3 below. In the topmost part of the lower layer (now shown in Fig. 7), where the most liquid water should reside, SNR is not sufficient to detect LDR. However, in the lower part of the layer the node (or subpeak) ice particles are likely contributing to this peak, making the LDR rather high. We expect that this is the case because the depolarizing prolate ice particles only affect the skewness of the respective node because freshly formed columns have vertical motions which are similar to the ones of the liquid droplets. We decided to not discuss this further in the manuscript.
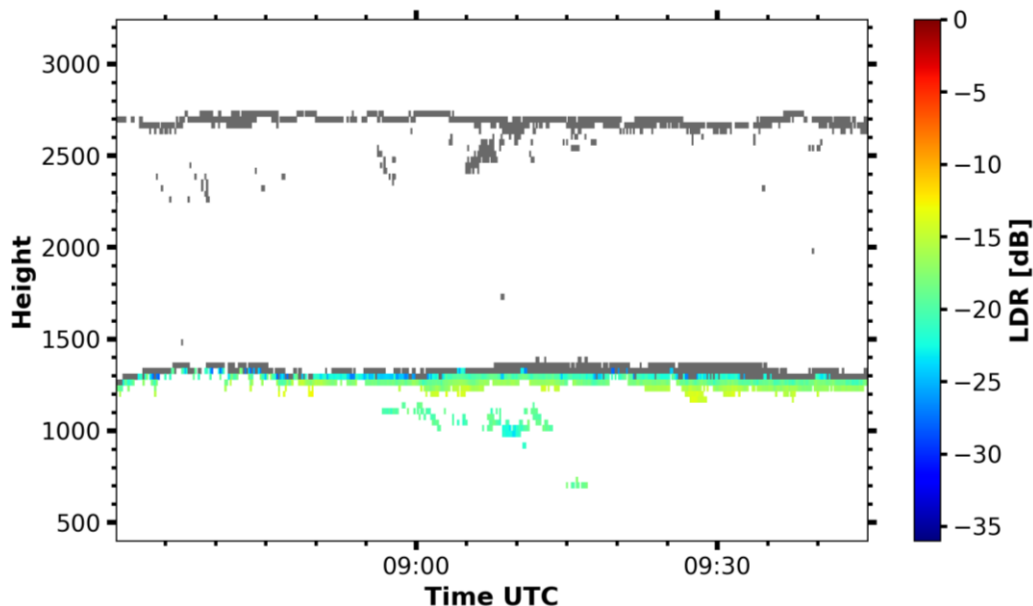
Fig 3 Linear depolarization ratio of the node detected as liquid containing (as Fig 7 in the new manuscript or Fig 4 in the old manuscript). Regions with insufficient signal for LDR estimation are marked in grey.

P9L3 "We cannot fully rule out that ice multiplication was triggered…": the authors should think about removing the following discussion because it is speculation and not of importance for this study.

We are confident, that the peakTree approach will be of considerable benefit for future studies of the microphysical structure of clouds. In order to emphasize this notion, we decided to add some discussion about possible microphysical processes to the text.

P9L14ff: It is a little challenging to follow which population the authors discuss.

Thanks for pointing to that hard to follow paragraph. We have added links to the discussed particle population (P12 L9, P12 L12, P13 L2, P13 L4).

P10 Fig 5: How many anchors were manually selected here?

As stated in the text, an anchor node every 50s and 150m. For Fig. 8 (former Fig. 5) it's then 720 nodes.

P10 Fig 6: P10 Fig 6: Given that IWC scales with Ze, I don't see a benefit of this figure.

We would like to point to the answer to Referee 1, who addressed a similar concern: "In the context of this paper, the IWC values are presented to give an impression on how the mass relation is between the single peaks. This is actually only possible if peaks were successfully separated first. Nevertheless, we decided to modify Fig 9 (former Fig. 6) in such a way that it now presents the total IWC (node 0) and the ratio of the IWC of the selected node to the total IWC."

P12L4: To my knowledge, microARSCL uses actually sub. I would recommend to focus stronger on the greater flexibility by overcoming the separation in noise separated and sub peaks.

We have removed the sentence on microARSCL and replaced it by (P16,L3ff): "The recursive structure of the tree allows to drop the artificial separation into noise-floor separated peaks and subpeaks within noise-floor separated peaks, as was necessary in prior approaches."

Appendix A: I would recommend adding a definition for spectral reflectivity.

We added a formula defining the spectral reflectivity (new Eq. A1).

P13L19: MIRA or Mira-35?

Changed to MIRA-35

peakTree: A framework for structure-preserving radar Doppler spectra analysis

Martin Radenz[1], Johannes Bühl[1], Patric Seifert[1], Hannes Griesche[1], and Ronny Engelmann[1]

[1]Leibniz Institute for Tropospheric Research (TROPOS), Leipzig, Germany

Correspondence: Martin Radenz (radenz@tropos.de)

Abstract. Clouds are frequently composed of more than one particle population even at smallest scales. Cloud radar observations ~~frequently~~ contain information on multiple particle species in the observation volume, when there are distinct peaks in the Doppler spectrum. ~~Complex multi-peaked~~ Multi-peaked situations are not ~~captured~~ taken into account by established algorithms, which are only using moments of the Doppler spectrum. In this study, we propose a new algorithm, that recursively represents the subpeaks as nodes in a binary tree. Using this tree data structure to represent the peaks of a Doppler spectrum it is possible to drop all a-priori assumptions on the number and arrangement of subpeaks. The approach is rigid, unambiguous and can provide a basis for advanced analysis methods. The applicability is briefly demonstrated in ~~a case study~~two case studies, where the tree structure was used to ~~separate two particle populations in an~~ investigate particle populations Arctic multi-layered mixed-phase ~~cloud, which was~~ clouds, which were observed during the research vessel Polarstern expedition PS106 and the Atmospheric Radiation Measurement Programs BAECC campaign.

1 Introduction

The characterization of mixed-phase clouds and associated microphysical processes poses a challenge to experimentalists, therefore these processes are still not well represented in general circulation models (Fan et al., 2011). In-situ instruments are subject to icing under the presence of supercooled liquid water, and the wide range of possible hydrometeor types require the deployment of instruments of which each can only cover a certain aspect of the whole hydrometeor distribution (Baumgardner et al., 2017; Korolev et al., 2017).

~~Frequently, cloud radars are~~ Cloud radars are frequently used for the investigation of mixed-phase clouds (Bühl et al., 2017). At Ka- and W-band, cloud radars are sensitive to scattering from the whole range of possible hydrometeors, ranging from cloud droplets to graupel (e.g. Kollias et al., 2007a; Fukao and Hamazu, 2014). In general, cloud radars are Doppler-capable and provide the backscattered signal as a function of Doppler velocity, commonly called Doppler spectrum (Wakasugi et al., 1986). When multiple particle populations are present in the observed volume, they are frequently represented as distinct peaks in the Doppler spectrum (e.g. Shupe et al., 2004; Luke et al., 2010; Verlinde et al., 2013; Yu et al., 2014; Kalesse et al., 2016; Kollias et al., 2016). The properties of a multi-peak situation can only partly be represented by the moments of a single peak algorithm, which causes errors in the target classification and subsequent microphysical retrievals. A multitude of approaches are available to classify clouds and retrieve water contents, particle sizes and number concentrations (for example Clothiaux

1

et al. 2000; Wang and Sassen 2002; Wang et al. 2004; Hogan et al. 2006; Illingworth et al. 2007; an overview is provided in Shupe et al. 2016 and Zhao et al. 2012). Almost all established algorithms are based on the assumption of mono-modal hydrometeor size distributions, which likely causes significant errors in multi-peaked situations.

The analysis of multi-peaked Doppler spectra can be separated into three steps:

1. **peak identification** (or peak finding): locate the boundaries of a (sub-)peak

2. **peak structuring**: identify the arrangement of the (sub-)peaks

3. **peak interpretation**: categorize the peaks and interpret them

Most available methods focus either on the peak identification or the peak interpretation step. For peak identification either noise-floor separated peaks and/or local minima in the spectral reflectivity are used (Shupe et al., 2004; Rambukkange et al., 2011). More sophisticated approaches allow for a separation of mono-modal peaks. This is done for example by using skewness signatures (Luke and Kollias, 2013) or continuous wavelet transforms (Luke et al., 2010; Yu et al., 2014). Recently Kalesse et al. (2019) proposed an algorithm for subjective peak identification criteria using machine learning.

~~When multi-peak situations are investigated, commonly strong assumptions are made on the structure of the Doppler spectrum, e.g. only one liquid and one ice peak (Shupe et al., 2004) or liquid, newly formed ice and ice from above (Rambukkange et al., 20~~ ~~. Relationships between subpeaks in neighboring Doppler spectra have to be interpreted manually. In more recent work, sophisticated methods were introduced to identify the liquid peak in a multipeak situation (Luke et al., 2010; Yu et al., 2014) or to separate the liquid peak from drizzle (Luke and Kollias, 2013).~~ Structure is reflected by a linear list of all subpeaks, usually sorted by velocity or reflectivity. In a further step, Oue et al. (2018), using the microARSCL algorithm (Kollias et al., 2007b; Luke et al., 2008), allow a primary peak to be split into two subpeaks~~, but the~~. But they constrain the structure by assuming the left peak (faster falling ~~) is assumed~~ peak) to have a higher reflectivity. Additionally, a noise-floor separated secondary peak is possible. ~~In summary, prior approached either used just a list of peaks (sorted by reflectivity or mean velocity) or a predefined structure based on strong assumptions on peak arrangement~~, but this one is assumed to be mono-modal. Such strong constraints may be justified for short periods at single geographic locations, but are not suitable for a general approach. Up to now, no generic and flexible formalism is available ~~,~~ to describe an arbitrary number of subpeaks of a Doppler spectrum without a-priori assumption on the structure.

In ~~this study it will~~ the peak interpretation step, the peaks are usually sorted into categories using their moments. Categories are for example one liquid and one ice peak (Shupe et al., 2004), liquid, newly formed ice, and ice from above (Rambukkange et al., 2011) or liquid and two ice populations (Oue et al., 2018).

This study will focus on the second step, peak structuring. It will be shown how a binary tree representation of multiple peaks can provide a rigid, hence flexible formalism ~~to represent~~ for structuring the peaks in a Doppler spectrum. The tree structure allows an arbitrary number of subpeaks in any arrangement, while at the same time being unambiguous and easily accessible by algorithms. The software implementing the algorithm is easily applicable to other radar systems and available openly. The study is structured as follows: The ~~dataset~~ datasets used for demonstration ~~of the tree generating peak-separation technique is~~

are introduced in Section 2. In Section 3, the ~~peak separation~~ binary tree peak structuring algorithm is presented. Section 4 is dedicated to the presentation of ~~a case study~~ two case studies in which the algorithm was used to ~~separate particle populations in an~~ investigate Arctic mixed-phase ~~cloud~~clouds. Discussions and conclusions are covered in Section 5.

2   ~~Dataset~~Datasets

5   The binary tree peak structuring algorithm is applied to two datasets using K_a band radars from different manufacturers with slightly different settings. Details on the instruments and datasets are given here.

2.1   MIRA-35 during PASCAL

During the Physical feedbacks of Arctic planetary boundary level Sea ice, Cloud and AerosoL (PASCAL) campaign (PS106; Wendisch et al., 2019) a cloud radar ~~Mira-35~~ MIRA-35 was operated as part of the OCEANET suite on R/V Polarstern
10   (Griesche et al., in preparation) together with, amongst other instruments, a Polly^{XT} Raman and polarization lidar (Engelmann et al., 2016) and a HATPRO 14-channel microwave radiometer (Rose et al., 2005). ~~Mira-35~~ MIRA-35 is a magnetron-based pulsed 35-GHz cloud radar with polarisation and Doppler capabilities (Görsdorf et al., 2015). During the campaign, ~~Mira-35~~ MIRA-35 was operated in linear-depolarization-ratio (LDR) mode. The pulse repetition frequency was $5\,\mathrm{kHz}$ and one Doppler spectrum was based on the fast Fourier transform of 256 pulses, yielding a Doppler resolution of $0.082\,\mathrm{m\,s^{-1}}$ ~~.~~ (Tab. 1). The
15   radar was operated in ~~vertical-stare~~ vertical pointing mode. It was based on a leveling platform which actively corrected for pitch and roll movement of the ship. Vertical movement of the radar was corrected at a rate of $4\,\mathrm{Hz}$ using the ship motion data originally recorded at $20\,\mathrm{Hz}$. For the datasets of Arctic clouds presented in here, the active stabilization was not available anymore due to a hardware failure. In the scope of this study, therefore the Doppler spectra acquired within $10\,\mathrm{s}$ were averaged incoherently to suppress the ship pitch and roll motion, while the vertical motion was still corrected at a rate of $4\,\mathrm{Hz}$. The lack
20   of active pitch and roll suppression lead to an accuracy of the zenith pointing of $1.5°$. For horizontal wind velocities below $10\,\mathrm{m\,s^{-1}}$, the bias introduced to the observed vertical velocity thus is below $0.2\,\mathrm{m\,s^{-1}}$.

By default, ~~Mira-35~~ MIRA-35 provides noise-cleaned compressed Doppler spectra (zspc) and moment data separately for meteorological targets and atmospheric plankton (Görsdorf et al., 2015). Further data analysis is subject to the operator of the cloud radar, to which the zspc data provides a solid base for potential application of peak separation techniques. Accurate
25   measurements of polarization variables, like the LDR, depend strongly on instrument hardware due to polarization leakage. This is especially true for spectral estimates of the LDR. The lowest LDR observable (integrated cross-polarization ratio ICPR) with this version of ~~Mira-35~~ MIRA-35 was estimated in the presence of light drizzle with the approach of Myagkov et al. (2015) and found to be $-27.6\,\mathrm{dB}$. A second effect that has to be considered while calculating the LDR, is the noise level in the cross channel. If the signal in the cross channel is below the noise level, the LDR is determined solely by the signal in the co
30   channel and no meaningful information on the polarization state of the received signal can be derived (Matrosov and Kropfli, 1993). Hence, when calculating the LDR (Eq. A6) only bins ~~with signal~~ where the signal in the cross channel is a factor of 3 above the noise level ~~in the cross-channel~~ are taken into account.

3

	PASCAL	BAECC
Type	MIRA-35	KAZR
Frequency	35 GHz	35 GHz
Pulse Length	200 ns	333 ns
Integration Time	10 s	6 s
No. Incoherent Averages	195	33
Pulse Repetition Frequency	5.0 kHz	2.8 kHz
N_{FFT}	256	512
Nyquist velocity v_{Nyq}	$10.5\,\mathrm{m\,s^{-1}}$	$5.9\,\mathrm{m\,s^{-1}}$
Velocity resolution	$0.082\,\mathrm{m\,s^{-1}}$	$0.023\,\mathrm{m\,s^{-1}}$

Table 1. Configuration settings of the two cloud radars used in this study.

2.2 KAZR during BAECC

The Biogenic Aerosols—Effects on Clouds and Climate (BAECC) campaign (Petäjä et al., 2016) was a deployment of the U.S. Department of Energy's Atmospheric Radiation Measurement (ARM) Mobile Facility (AMF) to Hyytiälä (61.9°N, 24.3°E), Finland from February to September 2014. A vertical looking KAZR 35 GHz cloud radar (Kollias et al., 2016) was part of the remote sensing instrumentation of the AMF. It was operated at a pulse repetition frequency of 2.8 kHz. The Doppler resolution is $0.023\,\mathrm{m\,s^{-1}}$, as a 512 point fast Fourier transform was used to estimate the Doppler spectra (Tab. 1). The vertically pointing KAZR used in this campaign does not posses a cross channel, hence no polarimetric variables are available.

3 Algorithm

3.1 Transforming the Doppler spectrum into the tree ~~representation~~structure

The algorithm explained in here transforms each Doppler spectrum with its (sub-)peaks into a full binary tree structure. A full binary tree is a directed graph with one root node and recursively each node might possess either two child nodes or none (Garnier and Taylor, 2009). ~~Here, a node~~ Each node can be identified by an index, which is based on level-order tree traversal. The index i of a node can be calculated by the following formulas:

$$i_{\mathrm{left\ child}} = 2\,i_{\mathrm{parent}} + 1 \tag{1}$$

$$i_{\mathrm{right\ child}} = 2\,i_{\mathrm{parent}} + 2 \tag{2}$$

$$i_{\mathrm{parent}} = \left\lfloor \frac{i_{\mathrm{child}} - 1}{2} \right\rfloor \tag{3}$$

4

These indices are illustrated in Fig. 1. This example shows a complete binary tree, meaning all nodes are present. When applied, some indices, e.g. 9 and 10 or 5, 6, 11, 12, 13 and 14 might be missing. However, the rule 'a node might possess either two child nodes or none' always holds.
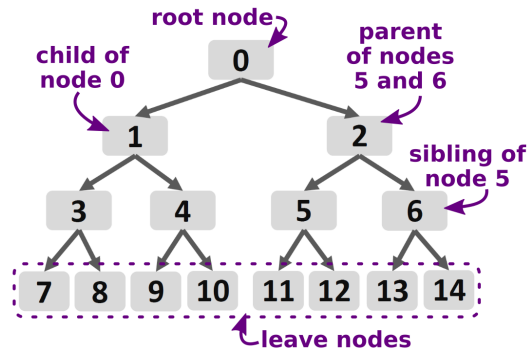
Figure 1. [new figure] Binary tree containing 15 nodes with possible indices according to level-order tree traversal.

Applied to radar Doppler spectra, a node is related to a part of the Doppler spectrum that contains at least one peak. ~~Starting~~
5 ~~from the noise-filtered~~ The peak boundaries are identified (step 1 as listed in Sec. 1) by a noise-floor threshold and local minima in the spectral reflectivity (or spectral power density)~~, the primary node contains the complete Doppler spectrum~~. These boundaries are then used to construct the tree structure (step 2 as listed Sec. 1). The root node contains all signal of the Doppler spectrum above the noise threshold between $-v_{\mathrm{Nyq}}$ and $+v_{\mathrm{Nyq}}$. ~~An example is~~ Two example spectra from KAZR and MIRA-35 are shown in Fig. 2 (a) ~~with the respective~~ and (b), respectively. The boundaries and moments for the MIRA-35
10 and KAZR are listed in Tab. 2 and 3, respectively. In a first step, all noise-floor-separated peaks are added as child nodes with their boundaries v_{left} and v_{right} (in the example ~~here -3.3 and $1.3\,\mathrm{m\,s^{-1}}$~~ for MIRA-35 -3.30 and $1.32\,\mathrm{m\,s^{-1}}$). Each node is then ~~searched for relative minima in spectral reflectivity. If a node contains internal minima and hence subpeaks, it needs to be splitted into child nodes. All found minima are sorted by the spectral reflectivity from lowest to highest~~ checked for (sub)-peaks within using the peak boundaries from the lowest to the highest spectral reflectivity. Starting with the lowest minimum at v_{add},
15 the node containing this minimum is split into two child nodes. When boundaries of the parent node are $[v_{\mathrm{left}}, v_{\mathrm{right}}]$, the left child node is $[v_{\mathrm{left}}, v_{\mathrm{add}}]$ and the right child node is $[v_{\mathrm{add}}, v_{\mathrm{right}}]$. In the example from Fig. 2 (a~~b~~) the internal minimum with the lowest spectral reflectivity is at ~~$-0.2\,\mathrm{m\,s^{-1}}$~~ $-0.25\,\mathrm{m\,s^{-1}}$ with a spectral reflectivity of $-33.4\,\mathrm{dBZ}$. This reflectivity also defines the threshold, that separates the subpeaks. The splitting at local minima is repeated for all remaining minima, always splitting the leaf node (i.e. a node that does not have any childs) in which the minimum is located.

20 A minimum is skipped, ~~when~~ if the prominence of ~~one~~ either of its subpeaks is less than $1\,\mathrm{dB}$~~, where prominence is the height of the peak above the~~. Prominence is the difference between the maximum spectral reflectivity of a subpeak and the threshold that is ~~definded by the local minimum (dashed grey lines in Fig 2 (a); similar to Shupe et al., 2004)~~ defined as by the spectral reflectivity at local minimum (dashed grey lines in Fig 2 (a, b); similar to Shupe et al., 2004).

Doppler spectrum

(a) KAZR
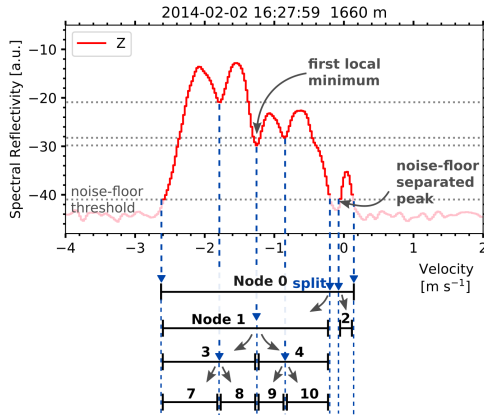
(b) MIRA-35
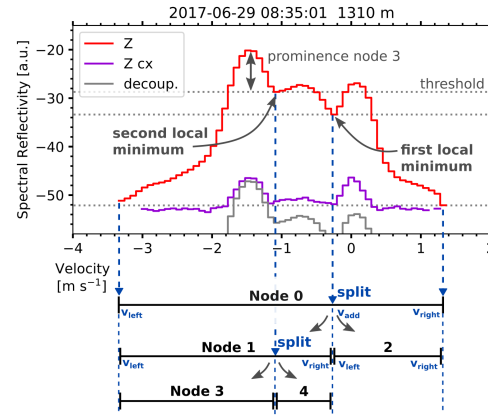
Binary tree structure in v-Z space

(c) KAZR
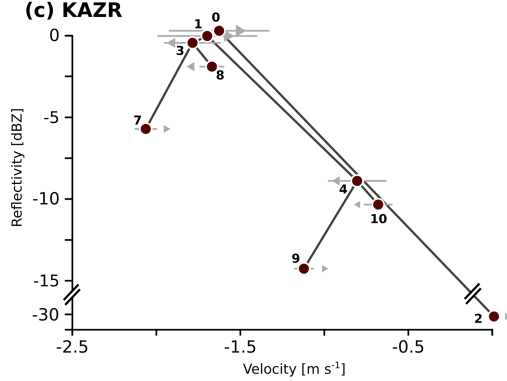
(d) MIRA-35
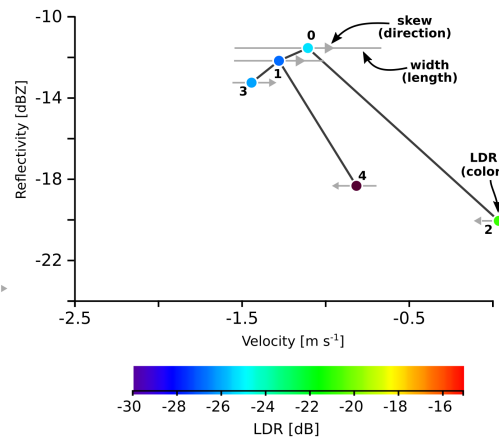
Figure 2. [updated figure] Example for generating the ~~tree from a~~ trees for two Doppler ~~spectrum. An example spectrum at 29 June 2017 08:35:01 UTC at 1310 m height is depicted in~~ spectra from different cloud radars of type KAZR (a, c) and MIRA-35 (b, d). The ~~primary~~ root node (Node 0) is splitted into child-nodes at the indicated velocity bins (dashed blue) which contain a local minimum in spectral reflectivity. The threshold defined by the noise-floor and the internal minima is marked with dashed grey lines. In the spectrum in (b) ~~shows~~ the reflectivity in the cross channel (Z cx) is shown together with the co channel signal subtracted by the polarization decoupling (further explanation in Sec. 2.1). (c) and (d) show the resulting ~~tree~~trees, where the location of a node in the v-Z space is based on its moments. Spectral width ~~and skewness are shown~~ is indicated quantitatively by the length of the grey lines and ~~triangles, respectively~~sign of the skewness is indicated by a triangle (pointing to left for negative skewness and vice-versa). The circle denoting the nodes position is color-coded in accordance to the nodes LDR.

Table 2. Moments for each peak from the MIRA-35 Doppler spectrum depicted in Fig. 2 (b) with the index of the node according to the level-order tree traversal and the boundaries $v_{\text{left}}, v_{\text{right}}$ are given in m s^{-1}. Child-nodes are denoted by their level of indentation. The units are dBZ for reflectivity Z and m s^{-1} for $\overline{v}$ and spectral width σ. The skewness γ is dimensionless, LDR is in dB. Both the threshold 'thres.' and the prominence 'prom.' are in dBZ.

~~Index~~ Node index	Boundaries $[v_{\text{left}}, v_{\text{right}}]$	Z	$\overline{v}$	σ	γ	LDR	thres.	prom.
0	`'−` [-3.30, 1.32]	-11.57	-1.10	0.59	1.01	-25.3	-52.1	32.0
1	`+−` [-3.30, -0.25]	-12.19	-1.27	0.36	1.08	-26.9	-33.4	13.2
3	`| +−` [-3.30, -1.07]	-13.27	-1.44	0.15	0.27	-26.1	-28.7	8.5
4	`| '−` [-1.07, -0.25]	-18.35	-0.81	0.16	-0.13	-32.2	-28.7	1.4
2	`'−` [~~-0.2, 1.3~~ -0.25, 1.32]	-20.08	0.04	0.13	-0.31	-20.9	-33.4	6.2

Table 3. Moments for each peak from the KAZR Doppler spectrum depicted in Fig. 2 (a) similar to Tab. 2

Node index	Boundaries $[v_{\text{left}}, v_{\text{right}}]$	Z	$\overline{v}$	σ	γ	thres.	prom.
0	`'−` [-2.58, 0.12]	0.78	-1.69	0.41	1.04	-41.0	28.2
1	`+−` [-2.58, -0.21]	0.78	-1.70	0.41	0.99	-41.0	28.2
3	`| +−` [-2.58, -1.26]	0.31	-1.80	0.27	-0.12	-29.8	17.0
7	`| | +−` [-2.58, -1.78]	-2.73	-2.04	0.11	0.28	-20.9	7.3
8	`| | '−` [-1.78, -1.26]	-2.61	-1.56	0.09	-0.25	-20.9	8.1
4	`| '−` [-1.26, -0.21]	-9.09	-0.81	0.23	-0.17	-29.8	7.2
9	`| | +−` [-1.26, -0.85]	-12.84	-1.04	0.09	0.25	-28.2	5.1
10	`| | '−` [-0.85, -0.21]	-11.38	-0.65	0.10	-0.18	-28.2	5.6
2	`'−` [-0.05, 0.12]	-28.06	0.04	0.04	-0.03	-41.0	5.7

In the next step, the moments of the Doppler spectrum (reflectivity, mean velocity, width, skewness) are calculated for each node within its boundaries $[v_{\text{left}}, v_{\text{right}}]$ (see Appendix A). ~~Only the part of the Doppler spectrum above the threshold defined by the spectral reflectivity minimum~~ Reflectivity factor Z is calculated by integrating the spectral reflectivity of the whole peak (i.e. from the noise-floor up). For all higher moments, signal below the threshold, that separated the ~~peaks are used.~~ (sub-)peak is neglected to avoid biases (see also Fig. A1). The LDR for ~~this~~ each node is calculated using the spectral reflectivity in the cross channel, if such a channel is available. Node 0 is similar to the moment estimation commonly used to analyze Doppler spectra (e.g. Carter et al., 1995; Clothiaux et al., 2000; Görsdorf et al., 2015). Its child nodes (1 and 2) are the subpeaks defined by the lowest relative minimum. The second lowest minimum then splits one of these nodes and gives nodes 3 and 4 (splitting node 1) or 5 and 6 (splitting node 2).

$$i_{\text{left child}} = 2\,i_{\text{parent}} + 1$$

$$i_{\text{right child}} = 2\,i_{\text{parent}} + 2$$

$$i_{\text{parent}} = \left\lfloor \frac{i_{\text{child}} - 1}{2} \right\rfloor$$

Furthermore, the The total number of subpeaks n_{subpeaks}, as estimated by established peak finding methods, can be calculated from the number of nodes n_{nodes}:

$$n_{\text{subpeaks}} = (n_{\text{nodes}} + 1)/2 \tag{4}$$

Each node is characterized by its reflectivity Z, vertical velocity v, spectral width, skewness, LDR and prominence. It is suitable to visualize the tree in the v-Z plane as a color-filled circle with the parent-child relationships depicted by a black line (Fig. 2 bc and d) and each circle is color-coded in accordance to its LDR (if available as for MIRA-35). The width and skewness are shown by a horizontal grey line and a grey triangle with varying size, respectively. This representation hence combines all key parameters of a multipeak Doppler spectrum.

3.2 ~~Grouping nodes into particle populations~~Peak interpretation

Once the tree structure is constructed various methods for peak interpretation can be used. In this study only two rather basic approaches are shown.

3.2.1 Selecting cloud droplet nodes

Nodes, that are most likely caused by liquid droplets can be identified by their moments, as done already in previous studies (e.g. Frisch et al., 1995; Shupe et al., 2001; Rambukkange et al., 2011; Yu et al., 2014; Kalesse et al., 2016). The liquid cloud droplets are assumed to be small and only possess a negligible terminal velocity. In the absence of strong vertical air motions the (sub-)peak caused by the liquid droplets will be close to $0\,\text{m}\,\text{s}^{-1}$. Additionally, due to their small size, the reflectivity of these droplets is rather small. Combining this to characteristics, a simple selection rule based on two thresholds: $Z < -20\,\text{dBZ}$ and $|v| < 0.3\,\text{m}\,\text{s}^{-1}$. Using this criteria, each node in a tree can be checked and the index of the fitting node is stored. This selection process can be used on larger time-height slices straightforward and computationally efficient, identifying regions of a cloud, where liquid droplets cause a distinguishable (sub-)peak.

3.2.2 Grouping nodes into particle populations

The nodes representing similar particle populations in neighboring (time-height) bins can be connected to obtain a continuous picture of the evolution of a particle population. First, a node is manually assigned to a particle population based on visual inspection and guided by the LDR value. These manually selected (anchor) nodes are spaced in steps of $50\,\text{s}$ and $150\,\text{m}$,
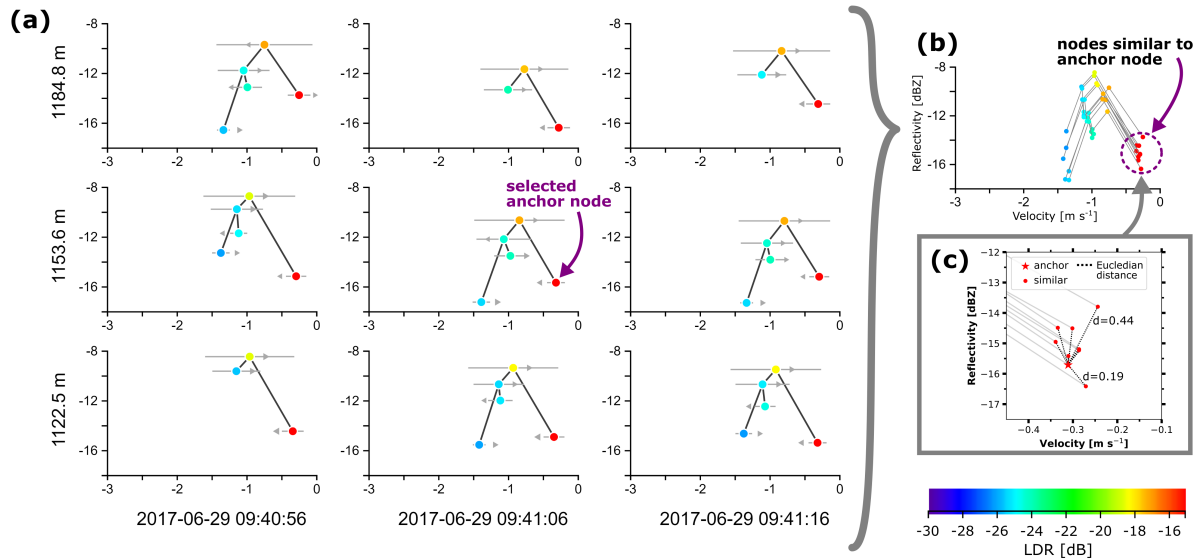
Figure 3. Illustration of the grouping algorithm for ~~a single step~~one anchor node. Single trees for a time-height slice of MIRA-35 observations are depicted in (a) with the selected anchor node marked by an arrow. The time-height cross section shown omits the outer trees of the 5×5 slice for clarity. The moments of each node are illustrated, as described in Fig. 2. In (b), the trees are combined into the same v-Z illustration with a circle denoting the nodes that are identified as similar by the Euclidean distance criterion. The Euclidean distance d is depicted in inset (c) for all nodes with index 2.

making one anchor representative for a slice of 5 ~~timestemps~~ time steps and 5 height bins or, in other words, for the 25 neighboring trees. For the time-height bins in between these anchor nodes, nodes with similar characteristics of the moments are automatically selected. Similarity is given, if a node is close to the anchor node in the v-Z space in minimal in terms of Euclidean distance d and below a threshold $d < 0.9$. ~~The~~ For the present study, the parameters Z and v are normalized by factors of 5 and 0.3 respectively, to make both comparable for the grouping algorithm (Fig. 3). The sibling of ~~these selected nodes~~ each selected node is afterwards assigned to the ~~second~~ complementary particle population.

4 Application~~: Separating two ice crystal habits in an Arctic cloud~~

~~On the~~

4.1 KAZR case, 02 February 2014: Identifying embedded liquid layers

On the 02 February 2014 an intense low pressure system over Faroe Islands together with a high pressure core above South-Western Russia caused southerly flow over Finland. Low level clouds were observed the whole day. During the afternoon a occluded front with cold frontal character reached the Hyytiälä field site. Frontal precipitation started at 14:30 UTC and was caused by two geometrically deep cloud systems, both topped at around 8 km height with a short pause in between. The first precipitation

event was characterized by liquid precipitation with a melting layer at around $1.2\,\mathrm{km}$ height (not shown), but for the second event from around 15:30 UTC onwards snow precipitation dominated. Fig. 4 shows a part of the frontal system. Between 16:00 and 16:20 UTC a lower cloud with almost constant cloud top at $2.6\,\mathrm{km}$ height was observed. In this cloud, reflectivity and vertical velocity are increasing toward the ground. At 16:18 UTC ice crystals from the top cloud start to sediment into this lower cloud. At $2.2\,\mathrm{km}$ height, the vertical velocity of these particles increases up to $-2.0\,\mathrm{m\,s^{-1}}$ (Fig. 4 b). The total number of nodes (Fig 4 c) reveals, that the cloud radar Doppler spectra were dominated by multi-peaked situations, predominantly in the lower layer. Up to 9 nodes were found, which corresponds to 5 subpeaks.

The selection rule described in Sec. 3.2.1 is now used to identify nodes, that are likely caused by liquid droplets. Fig. 5 shows the moments of the liquid droplet nodes. Two liquid layers become visible, a lower one between $0.8\,\mathrm{km}$ and $1.3\,\mathrm{km}$ height and a higher one with more irregular boundaries between $1.6\,\mathrm{km}$ and $2.6\,\mathrm{km}$ height. The vertical velocity (Fig 5) shows the typical pattern of small particles with negligible terminal fall velocity, which follow the air motion. Areas of up- and downdrafts with velocities between $-0.5\,\mathrm{m\,s^{-1}}$ and $+0.5\,\mathrm{m\,s^{-1}}$ are clearly visible.

4.2 MIRA-35 case, 29 June 2017: Separating two ice crystal populations in an Arctic cloud

On the 29 June 2017 R/V Polarstern was located a few nautical miles north of the island Kvitøya at $80.5°\mathrm{N}, 31.5°\mathrm{E}$ and operated in the frame of the PASCAL campaign. The synoptic situation was controlled by a low over Fram strait with a secondary low that passed Polarstern on that day with the surface wind veering from SE to NW and frequent light precipitation.

Between 08:30 and 09:45 UTC a cloud was continuously observed by ~~Mira-35~~ MIRA-35 from the surface up to $2.7\,\mathrm{km}$ height with a cloud top temperature of $-15°\mathrm{C}$ (see Fig. 6). The thermodynamic structure of the cloud was probed by a RS92-SGP radiosonde, that was launched from Polarstern at 10:50 UTC (Schmithüsen, 2017). The ~~humidity profile~~ spread between temperature and dewpoint (Fig. 6 a) shows saturation with respect to liquid water throughout the whole cloud. Very light precipitation was observed at the surface by an optical disdrometer (Klepp et al., 2018), peaking to $0.1\,\mathrm{mm\,h^{-1}}$ at 08:50 UTC. The highest values of liquid water path ($\sim 50\,\mathrm{g\,m^{-2}}$), obtained from the microwave radiometer (Rose et al., 2005), were also observed during this time. Low reflectivity and vertical velocities close to $0\,\mathrm{m\,s^{-1}}$ with alternating up- and downdrafts suggest the presence of a turbulent liquid layer capping the cloud. Below $1.3\,\mathrm{km}$ height, reflectivity and LDR of the single peak analysis show a sharp increase, giving hints to a change in microphysical properties, such as size or shape.

Application of the multi-peak analysis introduced above reveals ~~,~~ that multi-peak spectra were quite frequent (Fig. 6 f). ~~Nodes that are~~ Fig 7 shows the nodes identified as caused by liquid ~~layers can not be depicted directly, but previous studies used the simple criterion of low reflectivity and vertical velocity close to $0\,\mathrm{ms^{-1}}$ to identify regions of a cloud, where the presence of liquid is likely (e.g. Shupe et al., 2001; Rambukkange et al., 2011; Yu et al., 2014; Kalesse et al., 2016). The thresholds used here are $Z < -20\,\mathrm{dBZ}$ and $|v| < 0.3\,\mathrm{ms^{-1}}$. Obviously, this selection rule only applies, when the liquid peak is separated by a local minimum from the remainder of the Doppler spectrum. As shown in Fig 7, two~~ droplets according to the selection rule from Sec. 3.2.1. Two continuous liquid layers at almost constant heights were observed during the whole ~~case study. The top one~~ event. The uppermost layer at $2.7\,\mathrm{km}$ height topping the cloud is also visible in the ~~single~~ moments of the full spectrum. The ~~second one~~ lower layer at $1.3\,\mathrm{km}$ height, being hidden when only using the moments of the full spectrum. Furthermore,
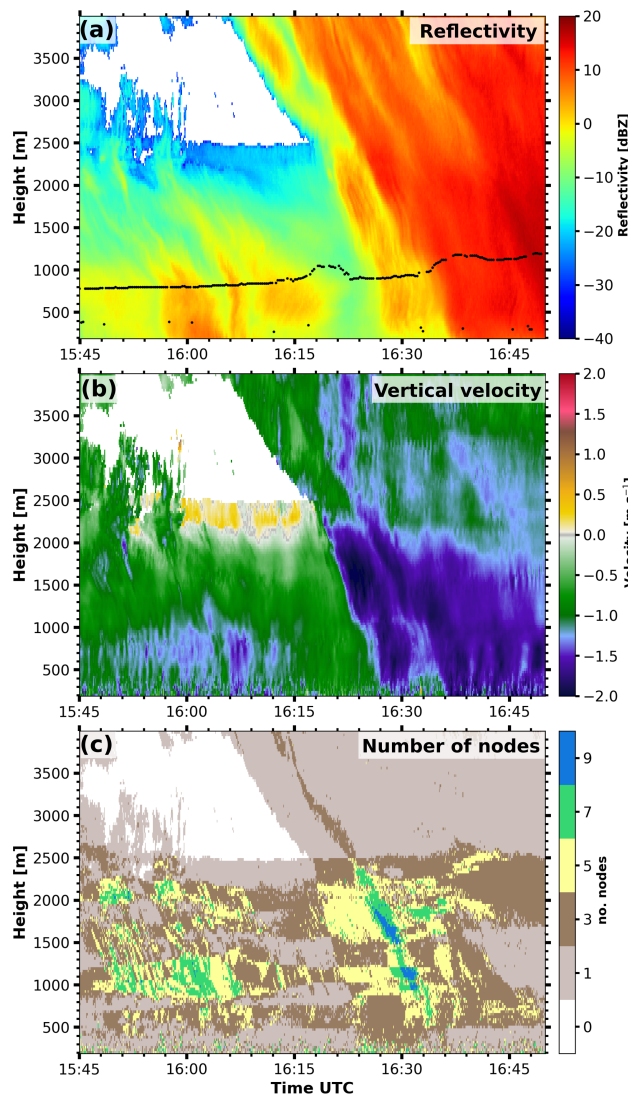
Figure 4. [new figure] KAZR reflectivity with lidar detected cloud base height (black dots, a), mean velocity (b) and number of nodes (c) at the 02 February 2014 from 15:45 to 16:45 UTC.

shorter periods ~~of~~ with likely liquid water presence were detected, for example from 08:55 to 09:15 UTC at $1.0\,\text{km}$ height. ~~Together with the lidar backscatter indicating a liquid cloud base~~ Additionally, the ceilometer-detected cloud base (Fig 7 a, black dots) indicates the base of the liquid layer at $750\,\text{m}$ height between 08:~~45~~ 40 and 09:~~10 (attenuated at lower heights during the remaining time, not shown), this suggests the presence of an extended liquid layer not clearly visible~~ 15 UTC. This lower part of the liquid layer did not produce a distinguishable (sub-)peak in the Doppler ~~spectra~~ spectrum and therefor no individual node.
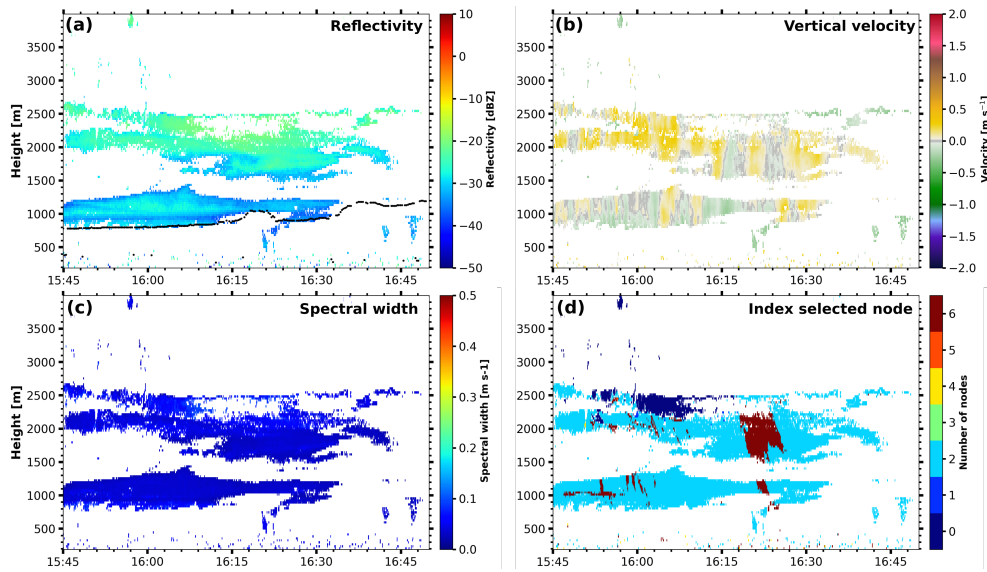
Figure 5. [new figure] KAZR reflectivity with lidar detected cloud base height (black dots, a), mean velocity (b), spectral width (c) and index of node (d) for nodes identified as liquid cloud drops at the 02 February 2014 from 15:45 to 16:45 UTC.

After grouping the nodes to particle populations (as explained in Section 3.2.2), the microphysical structure of this cloud becomes clearer. The faster-falling particle population (Fig. 8 left column) originating at the uppermost liquid layer at $2.7\,\mathrm{km}$ height has a rather variable reflectivity with background values of around $-20\,\mathrm{dBZ}$ and maxima in frequently occuring fall-streaks of up to $0\,\mathrm{dBZ}$ reflectivity. The vertical velocity (Fig. 8 c) is quite variable as well. Below $2.5\,\mathrm{km}$ height, the ~~generated~~

5   ~~ice particles descent~~ ice particles generated at cloud top descend with velocities of ~~0.5 and $2.0\,\mathrm{ms}^{-1}$~~ -0.5 and $-2.0\,\mathrm{m\,s}^{-1}$. The low LDR of these particles (Fig. 8 e) is characteristic for ~~prolate~~ oblate or plate-like particles (Myagkov et al., 2016), which is also consistent with particle ~~habits~~ shapes formed at cloud top temperatures of around $-15°\mathrm{C}$ (Bühl et al., 2016). Below the height of primary ice formation, several processes like depositional growth and and aggregation might contribute to particle growth.

10 Frequently, fallstreaks from the upper layer penetrate the second liquid layer at $1.3\,\mathrm{km}$ height. The lower-level liquid layer with a temperature of $-5°\mathrm{C}$ also continuously forms ice (Fig. 8 right column). The vertical velocity ~~is slower (-0.2 to $-0.7\,\mathrm{ms}^{-1}$~~ (Fig. 8 d) is lower (-0.2 to $-0.7\,\mathrm{m\,s}^{-1}$) and more homogeneous than for the other particle population. The high LDR of $-14\,\mathrm{dB}$ at heights of 100 to $200\,\mathrm{m}$ below the top of the liquid layer can be attributed to ~~columnar or needle-like~~ prolate or columnar ice crystals (Myagkov et al., 2016; Bühl et al., 2016). Hence, ice formation takes place between 1.1 and $1.3\,\mathrm{km}$ height, which is

15 also underpinned by the gradual increase of reflectivity and vertical velocity toward ground. Below $1.1\,\mathrm{km}$ height, the reflectivity is more variable, with maxima of $9\,\mathrm{dBZ}$ at 08:50 UTC and minima of $-11\,\mathrm{dBZ}$ at around 09:10 UTC. We ~~cannot~~ can not fully rule out from the information given, that ice multiplication was triggered when the higher-level ice particles descended into the lower liquid layer. However, ice was formed from the lower liquid layer constantly over time (Fig. 8 right column),

12
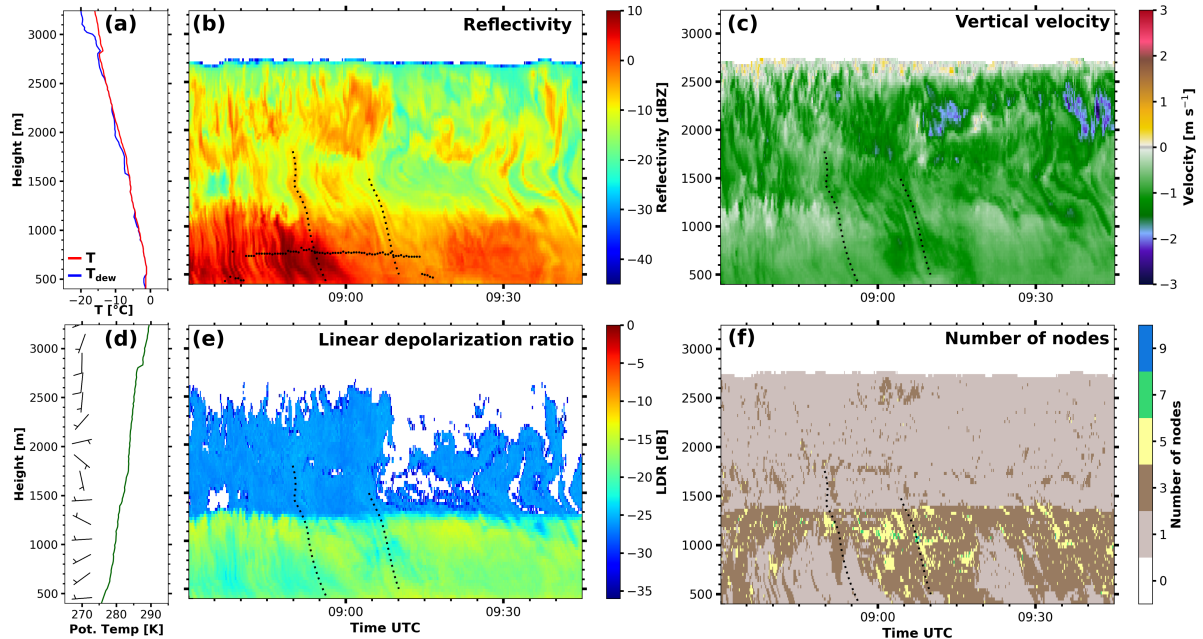
Figure 6. [updated figure] Radiosonde ascend at the 29 June 2017 10:50 UTC (a, d from Schmithüsen, 2017). ~~Mira-35~~ MIRA-35 reflectivity with lidar detected cloud base height (black dots, b), mean velocity (c) and linear depolarization ratio (e) of the zeroth node (moments of the single peak analysis) at the 29 June 2017 from 08:30 to 09:45 UTC. Total number of nodes (f) for the same period.

even in periods where particles with very low reflectivity were potentially seeding from above, as it was the case for example between 09:10 und 09:30 UTC~~, which~~. This supports the interpretation, that at least a few ice crystals were caused by primary ice formation.

Looking into two individual fallstreaks, it is possible to track the evolution of the two particle populations. The selected fallstreaks are illustrated as black dashed curves in Fig. 8. In the frame of this study, the fallstreaks were selected manually based on the criteria of following the ~~signal~~ maximum of the radar reflectivity of the faster falling particle population. It should be noted, that techniques for an automated classification of fallstreaks exist (Kalesse et al., 2016; Pfitzenmaier et al., 2017), which should be applied when longer time series are analysed. But these algorithms have shortcomings when strong directional wind shear is present, as in this case (Fig. 6 d). First hints for different microphysical processes become evident from tracking the properties of the individual nodes in the selected fallstreaks. The first one starts at 08:52 UTC and $1.8\,\text{km}$ height with ~~a~~ oblate particles having rather constant reflectivity of $-5\,\text{dBZ}$ and a vertical velocity of around ~~$-1.0\,\text{ms}^{-1}$~~ $-1.0\,\text{m s}^{-1}$. The reflectivity of this population is almost constant down to $0.9\,\text{km}$ height, even after the fallstreak reaches the lower liquid layer. The LDR is unaffected by the liquid layer as well. Contrarily, the prolate particle population generated within this liquid layer shows a strong increase in reflectivity from $-20\,\text{dBZ}$ to $+6\,\text{dBZ}$, while LDR decreases from $-14\,\text{dB}$ to $-19\,\text{dB}$. Below $0.8\,\text{km}$

13
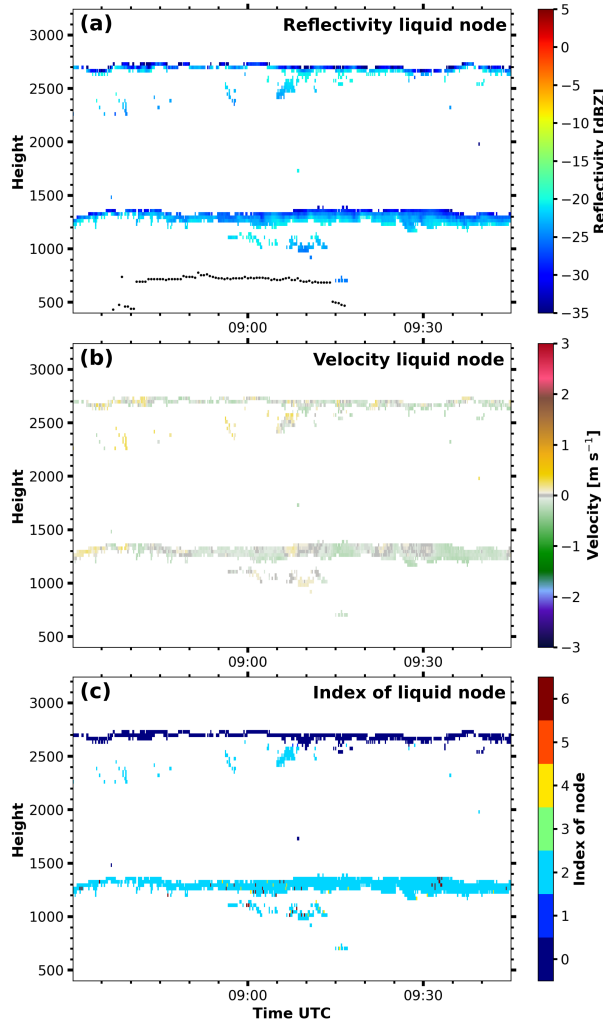
Figure 7. [updated figure] ~~Reflectivity~~ MIRA-35 reflectivity with lidar detected cloud base height (black dots, a), mean velocity (b) and index of node (c) for nodes identified as ~~supercooled~~ liquid cloud drops by the selection rule from Sec. 3.2.1 at the 29 June 2017 from 08:30 to 09:45 UTC.

height, the faster falling mode is not longer visible as a separate peak (and accordingly the node disappears), because the slower falling population becomes dominant in the Doppler spectrum.

The second fallstreak, being less pronounced than the first one, begins at 09:06 UTC and 1.5 km height with a reflectivity of -10 dBZ and again a vertical velocity of around ~~$-1.0\,\mathrm{m\,s}^{-1}$~~ $-1.0\,\mathrm{m\,s}^{-1}$ for the oblate particles. After reaching the liquid layer

5   at 1.3 km height, the reflectivity of this particle population increases to -7 dBZ and also the velocity increases slightly. The LDR remains below -25 dB. The second particle population with a prolate shape grows as well. From less than -20 dBZ in the liquid layer to -4 dBZ at 0.6 km with a final velocity of ~~$-0.6\,\mathrm{m\,s}^{-1}$~~ $-0.6\,\mathrm{m\,s}^{-1}$. During this growth, LDR remains at the high

value of $-14\,\text{dB}$, indicating no change ~~in particle habit~~of the particle shape. Due to insufficient polarimetric data, especially the lack of scans, it is difficult to disentangle the contribution of different microphysical processes to particle growth. A more detailed investigation, using synergistic retrievals on top of the algorithm presented here, is required to pin-down the relevant processes further.

5   The ice water content (IWC) for each particle population can be retrieved from Z and the temperature (Hogan et al., 2006). This $Z-T$ retrieval was developed under the assumption of mono-modal peaks in the Doppler spectrum, but using the tree structure it is possible to include the information from the Doppler spectrum into this retrieval rather easily. Fig. 9 shows the IWC for node 0 or the full Doppler spectrum (a), hence assuming single-peaked spectra~~, and for the two~~. Applying the IWC retrieval for the separated particle populations ~~(b, c). This opens the possibility to estimate the IWC for individual particle~~

10 ~~populations using established retrievals.~~ reveals the relative contribution of one population to total ice mass (Fig. 9 b). As could also be seen in the discussion on the reflectivity of the particle populations above, the precipitation reaching the ground between 08:30 and 09:00 UTC could not be directly linked to cloud top (2.7 km), ~~but was strongly modified by the internal liquid layer at~~ as the whole ice mass below 1.3 km height ~~.~~ can be assigned to the prolate particle population. Contrarily between 09:00 and 09:15 ice mass was almost equally distributed to both particle populations below 1.3 km height. Following this approach, the

15 proposed technique can also be used to extend the capabilities of other established retrieval algorithms.

5   Discussion and Conclusions

We proposed a binary tree structure for individual peaks of a multi-peaked cloud radar Doppler spectrum. This data structure does not require prior assumptions on the arrangement or hierarchy of the peaks. The tree structure allows to select the level of complexity with which the Doppler spectrum is approximated, by the number of nodes taken into account. It also pro-

20 vides backward compatibility, as the root node (i.e. node 0) holds the moments of the full Doppler spectrum with an implicit assumption of mono-modality. These moments are similar to standard Doppler spectra processing. Hence, a seamless transition from current single-peak techniques to multi-peak analysis is possible. ~~This is an improvement compared, for example to microARSCL, where usually the primary peak (noise-floor separated peak with the maximum of spectral reflectivity) is used to represent the~~ The recursive structure of the tree allows to drop the artificial separation into noise-floor separated peaks and

25 subpeaks within noise-floor separated peaks, as was necessary in prior approaches (see Fig 13 in Williams et al., 2018). This separation imposed strong constraints on structure, without having a physical reason. For example, depending on the intensity of turbulence, two noise-floor separated peaks might appear only as (sub-)peaks of one peak in the Doppler spectrum.

    We showed two basic techniques to demonstrate, how the tree structure can be utilized for peak interpretation (step 3 as defined in Sec. 1). The first technique used a simple selection rule to identify peaks that most likely are caused by liquid water.

30 The choice of the threshold is based on prior studies. For reflectivity, the $-20\,\text{dBZ}$ threshold as used by Oue et al. (2018) or reported by Kalesse et al. (2016), is rather conservative compared to older studies (e.g. Frisch et al., 1995; Kogan et al., 2005; Yu et al., 201 . The velocity threshold depends strongly on dynamical environment. The threshold of $|v| < 0.3\,\text{m\,s}^{-1}$ might only be valid for stratiform conditions, as in the two case studies shown. Good agreement with the ceilometer-derived cloud base heights in the
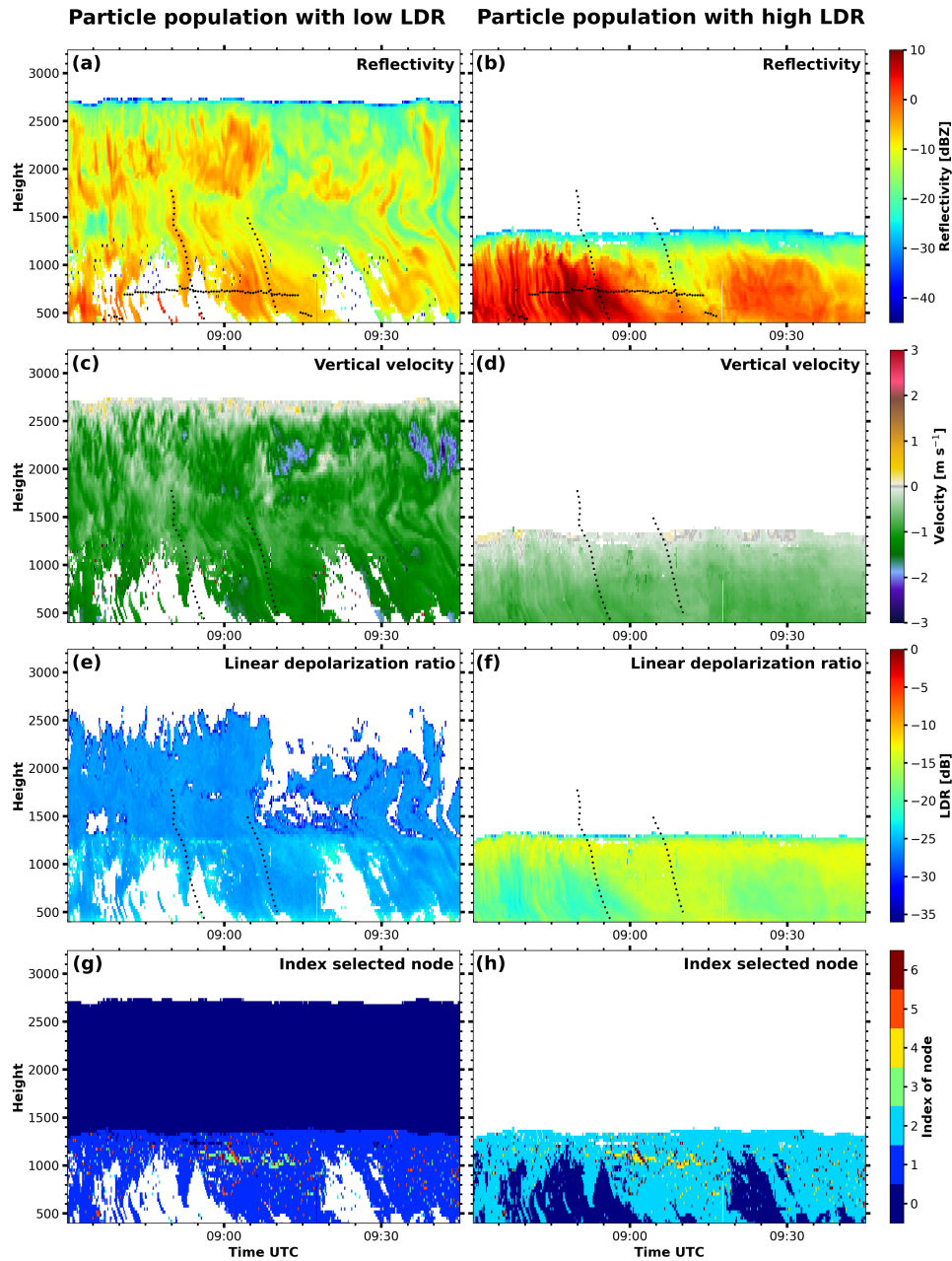
Figure 8. **[updated figure]** ~~Reflectivity~~ MIRA-35 reflectivity with lidar detected cloud base height (black dots, a, b), mean velocity (c, d), linear depolarization ratio (LDR; e, f) and index of the selected node (g, h) of the two particle populations (left and right column) at the 29 June 2017 from 08:30 to 09:45 UTC. The dashed black lines locate the two fallstreaks described in the text. For regions marked in white no node could be assigned to the respective particle population.
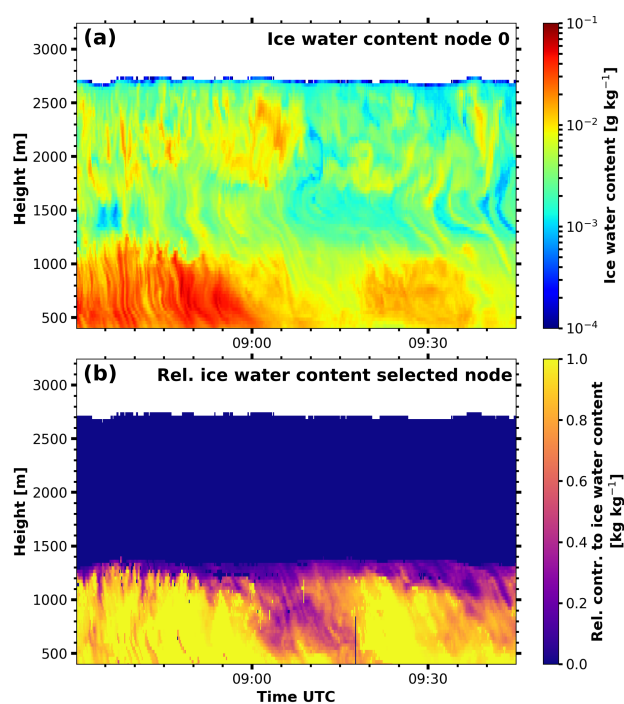
Figure 9. [updated figure] Retrieved ice water content from ~~the full Doppler spectrum~~ node 0 (a) and the ~~two separated~~ relative contribution of the particle ~~populations~~ population with high LDR (b~~, c~~) at the 29 June 2017 from 08:30 to 09:45 UTC.

KAZR case (Sec. 4.1) is in agreement for other studies using comparable threshold. Similar rules can potentially be applied for other particle types with a clear signature in the moments of the ~~full spectrum~~ Doppler spectrum, as it might be for example be the case for heavily rimed particles.

~~In a second step we demonstrated a simple application this new structure by grouping~~ The second technique grouped nodes from neighboring Doppler spectra into particle populations based on their moments using the Euclidean distance in v-Z space. The thresholds used here depend strongly on the conditions they are applied to. The normalization factors for reflectivity Z and velocity v weight the variation in one dimension with respect to the other. For this case, changes in velocity were only allowed to be relatively small compared to changes in reflectivity. Considering only changes along one axis, reflectivity could vary by $4.5\,\mathrm{dBZ}$ for neighboring trees for two nodes still be considered to belong to the same particle population, whereas velocity could only vary by $0.27\,\mathrm{m\,s^{-1}}$. The distance threshold d controls gaps in the grouping. A low distance threshold would select only a subset of nodes, introducing gaps in time and range for the grouped particle population. A high distance threshold can make the selection ambiguous, as two or more nodes in one tree might fulfill this condition. The frequency of anchor nodes is controlled by the evolution of the cloud. When rapid changes are expected, as for example in more convective situations, more anchor nodes will be required. In this study, the anchor nodes had to be selected manually, but automatizing this selection should be also possible in a future step.

The ~~technique was demonstrated by separating and sorting nodes into two particle populations in~~ binary tree peak structuring algorithm together with the interpretation techniques was applied to mixed-phase cloud cases observed by two different cloud radar systems. The liquid node selection rule (Sec. 3.2.1) was applied to to case studies from both campaigns. In the KAZR case study from the BAECC campaign multi-peaked Doppler spectra were quite frequent (Sec. 4.1). Selecting the nodes that were likely caused by liquid droplets revealed two liquid layers. The base of the lower layer at $800\,\mathrm{m}$ was also observed by a collocated ceilometer. In the MIRA case (Sec. 4.2), the liquid droplets detected at cloud base at around $750\,\mathrm{m}$ height did not form a distinct peak and can not be identified by this basic approach. More sophisticated peak identification methods (step 1 as defined in Sec. 1) could be used to address this issue.

The grouping technique (Sec. 3.2.2) was demonstrated in a second case of an Arctic mixed-phase cloud, where nodes were separated and sorted into two particle populations. Looking at both particle populations individually ~~can provide~~ provides deeper insights into the prevalent physical processes. The upper liquid layer formed ice particles of, most likely, oblate shape as indicated by the LDR. While sedimenting, these particles grew further, either due to water vapor deposition or aggregation. When reaching a second liquid layer below, riming becomes available as a potential third growth process. Within this liquid layer, a new ice particle population emerges. Using the tree representation of multi-peaked Doppler spectra, we were able to identify this second liquid layer and individually track the evolution of the upper-level and the new ice particle population. Indications are given that new particles are formed: (1) the LDR signatures point toward prolate particles, which fits to the temperature in the second liquid layer and (2) ice is also produced in regions where ice fallstreaks from above are absent.

Nevertheless, the characterization of the interactions between the two populations and further narrowing-down relevant growth processes would require a more-detailed investigation based on polarimetry or multi-wavelength radar and lidar synergy, which is beyond the scope of the current study. Furthermore, this case study covers situations, where the assumption of the fastest falling subpeak was not the one with the highest reflectivity, as done by Oue et al. (2018), was violated.

In summary, we consider the ~~peakTree approach~~ binary tree peak structuring algorithm a well-suited ~~technique~~ approach for enhancing the capabilities of cloud ~~radar for the~~ radars for the analysis of multi-peaked spectra, especially the characterization of mixed-phase cloud processes. Tracing the evolution of polarimetric properties and velocity of distinct nodes will allow much more detailed studies of the ice growth and ice multiplication processes in future.

It is feasible to apply the algorithm also to Doppler spectra of ~~other Doppler~~ further radars, as only very few parameters, namely the number of incoherent averages, the prominence, the noise threshold and - if a cross channel is available - the ICPR, need to be adjusted. ~~Another extension would be to use~~

This study used rather basic techniques for peak identification and interpretation (steps 1 and 3 as listed in Sec. 1). Both issues can be addressed in further work, but keeping the tree structure as a connection. For example other peak finding algorithms ~~as an input for the tree generation~~ can easily be used to replace the minimum in spectral reflectivity approach used here. The only information required to build the tree are at which Doppler bins the Doppler spectrum should be splitted. ~~Furthermore~~With respect to the interpretation step, the tree structure can extend the capabilities of established classification algorithms and microphysical retrievals. Many of these methods are based on single moment data and hence a mono-modal assumption. By

applying the retrieval to each node individually, the strong assumption of mono-modality could be relaxed without major adjustments in the retrieval algorithm itself, as shown for the $Z-T$ ice water content retrieval.

Appendix A: Formulas for calculating the moments

The moments for each node in the Doppler spectrum are calculated following the formulas given by Maahn and Löhnert (2017), Radenz et al. (2018) and Williams et al. (2018). $S(v)$ denotes the spectral reflectivity in the co channel with the instrument weighting function $I(\boldsymbol{r}_0, \boldsymbol{r})$ (Doviak and Zrnic, 1993), the center of the range gate $\boldsymbol{r}_0$, the observation volume V, the wavelength of the radar λ and the dielectric factor K.

$$S(\boldsymbol{r}_0, v) = \frac{\lambda^4}{\pi^5 |K|^2} \int_V I(\boldsymbol{r}_0, \boldsymbol{r}) \eta'(\boldsymbol{r}, v)\,\mathrm{d}^3 \boldsymbol{r}. \tag{A1}$$

The spectrum is expressed in terms of equivalent reflectivity factor, relating the volume reflectivity η' to the reflectivity factor Z_e assuming Rayleigh scattering by water droplets. For brevity 'factor' behind reflectivity and the subscript e are omitted. The cloud radar samples the Doppler spectrum at discrete velocity bins determined by the number of points in the fast Fourier transformation. Hence, $S(v)$ is represented as $S(i)$, where $v(i)$ maps the bin index to the velocity. The peak boundaries are $v_{\text{left}} = v(l), v_{\text{right}} = v(r)$. $\overline{v}$ is the mean velocity, σ the spectral width and γ the skewness. For higher-order moments, tails of signal on side of the peak might cause a bias, when the other side is bound by an internal minimum (Fig. A1). To prevent this, only spectral reflectivity values $S(i)$ above the threshold that separates the (sub-)peak from its neighbor are included for calculating moments other than Z.

$$Z = 10 \log_{10} \sum_{i=l}^{r} S(i) \tag{A2}$$

$$\overline{v} = \frac{\sum\limits_{i=l}^{r} S(i)\, v(i)}{\sum\limits_{i=l}^{r} S(i)} \tag{A3}$$

$$\sigma^2 = \frac{\sum\limits_{i=l}^{r} S(i)\, [v(i) - \overline{v}]^2}{\sum\limits_{i=l}^{r} S(i)} \tag{A4}$$

$$\gamma = \frac{\sum\limits_{i=l}^{r} S(i)\, [v(i) - \overline{v}]^3}{\sigma^3 \sum\limits_{i=l}^{r} S(i)} \tag{A5}$$

5   The LDR is calculated by using the spectral reflectivity in the cross channel $S_{cx}(i)$:

$$\mathrm{LDR} = 10 \log_{10} \frac{\sum\limits_{i=l}^{r} S_{cx}(i)}{\sum\limits_{i=l}^{r} S(i)} \tag{A6}$$
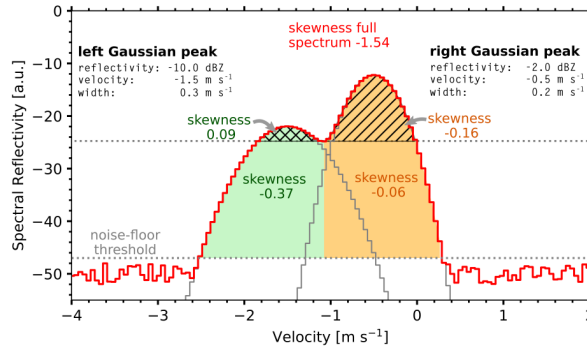
Figure A1. [new figure] Example for different skewness values, if the spectrum is cut at the local minimum or not.

References

Baumgardner, D., Abel, S. J., Axisa, D., Cotton, R., Crosier, J., Field, P., Gurganus, C., Heymsfield, A., Korolev, A., Krämer, M., Lawson, P., McFarquhar, G., Ulanowski, Z., and Um, J.: Cloud Ice Properties: In Situ Measurement Challenges, Meteorological Monographs, 58, 9.1–9.23, https://doi.org/10.1175/AMSMONOGRAPHS-D-16-0011.1, 2017.

5   Bharadwaj, N., Matthews, A., Nelson, D., Lindenmaier, I., Isom, B., Hardin, J., and Johnson, K.: Atmospheric Radiation Measurement (ARM) user facility, updated hourly. Ka ARM Zenith Radar (KAZRSPECCMASKGECOPOL). 2014-02-02 to 2014-02-03, ARM Mobile Facility (TMP) U. of Helsinki Research Station (SMEAR II), Hyytiala, Finland; AMF2 (M1), https://doi.org/http://dx.doi.org/10.5439/1025218, 2014.

Bühl, J., Alexander, S., Crewell, S., Heymsfield, A., Kalesse, H., Khain, A., Maahn, M., Van Tricht, K., and Wendisch, M.: Remote Sensing,
10 Meteorological Monographs, 58, 10.1–10.21, https://doi.org/10.1175/AMSMONOGRAPHS-D-16-0015.1, 2017.

Bühl, J., Seifert, P., Myagkov, A., and Ansmann, A.: Measuring ice- and liquid-water properties in mixed-phase cloud layers at the Leipzig Cloudnet station, Atmospheric Chemistry and Physics, 16, 10 609–10 620, https://doi.org/10.5194/acp-16-10609-2016, 2016.

Carter, D. A., Gage, K. S., Ecklund, W. L., Angevine, W. M., Johnston, P. E., Riddle, A. C., Wilson, J., and Williams, C. R.: Developments in UHF lower tropospheric wind profiling at NOAA's Aeronomy Laboratory, Radio Science, 30, 977–1001,
15 https://doi.org/10.1029/95RS00649, 1995.

Clothiaux, E. E., Ackerman, T. P., Mace, G. G., Moran, K. P., Marchand, R. T., Miller, M. A., and Martner, B. E.: Objective Determination of Cloud Heights and Radar Reflectivities Using a Combination of Active Remote Sensors at the ARM CART Sites, Journal of Applied Meteorology, 39, 645–665, https://doi.org/10.1175/1520-0450(2000)039<0645:ODOCHA>2.0.CO;2, 2000.

Doviak, R. J. and Zrnic, D. S.: Doppler Radar & Weather Observations, Courier Corporation, https://doi.org/10.1016/C2009-0-22358-0,
20 1993.

Engelmann, R., Kanitz, T., Baars, H., Heese, B., Althausen, D., Skupin, A., Wandinger, U., Komppula, M., Stachlewska, I. S., Amiridis, V., Marinou, E., Mattis, I., Linné, H., and Ansmann, A.: The automated multiwavelength Raman polarization and water-vapor lidar Polly^{XT}: the neXT generation, Atmospheric Measurement Techniques, 9, 1767–1784, https://doi.org/10.5194/amt-9-1767-2016, https://www.atmos-meas-tech.net/9/1767/2016/, 2016.

25 Fan, J., Ghan, S., Ovchinnikov, M., Liu, X., Rasch, P. J., and Korolev, A.: Representation of Arctic mixed-phase clouds and the Wegener-Bergeron-Findeisen process in climate models: Perspectives from a cloud-resolving study, Journal of Geophysical Research: Atmospheres, 116, https://doi.org/10.1029/2010JD015375, 2011.

Frisch, A. S., Fairall, C. W., and Snider, J. B.: Measurement of Stratus Cloud and Drizzle Parameters in ASTEX with a Ka-Band Doppler Radar and a Microwave Radiometer, Journal of the Atmospheric Sciences, 52, 2788–2799, https://doi.org/10.1175/1520-
30 0469(1995)052<2788:MOSCAD>2.0.CO;2, 1995.

Fukao, S. and Hamazu, K.: Radar for Meteorological and Atmospheric Observations, Springer, https://doi.org/10.1007/978-4-431-54334-3, 2014.

Garnier, R. and Taylor, J.: Discrete Mathematics: Proofs, Structures and Applications, Third Edition., CRC Press, Hoboken, 2009.

Griesche, H., Seifert, P., Baars, H., Engelmann, R., Radenz, M., Ansmann, A., and Macke, A.: Application of the shipborne remote-sensing
35 supersite OCEANET for profiling of Arctic aerosols and clouds during Polarstern cruise PS106, 0, null, https://doi.org/-, in preparation.

Görsdorf, U., Lehmann, V., Bauer-Pfundstein, M., Peters, G., Vavriv, D., Vinogradov, V., and Volkov, V.: A 35-GHz Polarimetric Doppler Radar for Long-Term Observations of Cloud Parameters—Description of System and Data Processing, Journal of Atmospheric and Oceanic Technology, 32, 675–690, https://doi.org/10.1175/JTECH-D-14-00066.1, 2015.

Hogan, R. J., Mittermaier, M. P., and Illingworth, A. J.: The Retrieval of Ice Water Content from Radar Reflectivity Factor and Temperature and Its Use in Evaluating a Mesoscale Model, Journal of Applied Meteorology and Climatology, 45, 301–317, https://doi.org/10.1175/JAM2340.1, 2006.

Illingworth, A. J., Hogan, R. J., O'Connor, E. J., Bouniol, D., Delanoë, J., Pelon, J., Protat, A., Brooks, M. E., Gaussiat, N., Wilson, D. R., Donovan, D. P., Baltink, H. K., van Zadelhoff, G.-J., Eastment, J. D., Goddard, J. W. F., Wrench, C. L., Haeffelin, M., Krasnov, O. A., Russchenberg, H. W. J., Piriou, J.-M., Vinit, F., Seifert, A., Tompkins, A. M., and Willén, U.: Cloudnet: Continuous Evaluation of Cloud Profiles in Seven Operational Models Using Ground-Based Observations, Bulletin of the American Meteorological Society, 88, 883–898, https://doi.org/10.1175/BAMS-88-6-883, 2007.

Kalesse, H., Szyrmer, W., Kneifel, S., Kollias, P., and Luke, E.: Fingerprints of a riming event on cloud radar Doppler spectra: observations and modeling, Atmospheric Chemistry and Physics, 16, 2997–3012, https://doi.org/10.5194/acp-16-2997-2016, 2016.

Kalesse, H., Vogl, T., Paduraru, C., and Luke, E.: Development and validation of a supervised machine learning radar Doppler spectra peak finding algorithm, Atmospheric Measurement Techniques Discussions, 2019, 1–37, https://doi.org/10.5194/amt-2019-48, 2019.

Klepp, C., Michel, S., Protat, A., Burdanowitz, J., Albern, N., Kähnert, M., Dahl, A., Louf, V., Bakan, S., and Buehler, S. A.: Ocean-RAIN, a new in-situ shipboard global ocean surface-reference dataset of all water cycle components, Scientific Data, 5, 180 122, https://doi.org/10.1038/sdata.2018.122, 2018.

Kogan, Z. N., Mechem, D. B., and Kogan, Y. L.: Assessment of variability in continental low stratiform clouds based on observations of radar reflectivity, Journal of Geophysical Research: Atmospheres, 110, https://doi.org/10.1029/2005JD006158, 2005.

Kollias, P., Clothiaux, E. E., Miller, M. A., Albrecht, B. A., Stephens, G. L., and Ackerman, T. P.: Millimeter-Wavelength Radars: New Frontier in Atmospheric Cloud and Precipitation Research, Bulletin of the American Meteorological Society, 88, 1608–1624, https://doi.org/10.1175/BAMS-88-10-1608, 2007a.

Kollias, P., Miller, M. A., Luke, E. P., Johnson, K. L., Clothiaux, E. E., Moran, K. P., Widener, K. B., and Albrecht, B. A.: The Atmospheric Radiation Measurement Program Cloud Profiling Radars: Second-Generation Sampling Strategies, Processing, and Cloud Data Products, Journal of Atmospheric and Oceanic Technology, 24, 1199–1214, https://doi.org/10.1175/JTECH2033.1, 2007b.

Kollias, P., Clothiaux, E. E., Ackerman, T. P., Albrecht, B. A., Widener, K. B., Moran, K. P., Luke, E. P., Johnson, K. L., Bharadwaj, N., Mead, J. B., Miller, M. A., Verlinde, J., Marchand, R. T., and Mace, G. G.: Development and Applications of ARM Millimeter-Wavelength Cloud Radars, Meteorological Monographs, 57, 17.1–17.19, https://doi.org/10.1175/AMSMONOGRAPHS-D-15-0037.1, 2016.

Korolev, A., McFarquhar, G., Field, P. R., Franklin, C., Lawson, P., Wang, Z., Williams, E., Abel, S. J., Axisa, D., Borrmann, S., Crosier, J., Fugal, J., Krämer, M., Lohmann, U., Schlenczek, O., Schnaiter, M., and Wendisch, M.: Mixed-Phase Clouds: Progress and Challenges, Meteorological Monographs, 58, 5.1–5.50, https://doi.org/10.1175/AMSMONOGRAPHS-D-17-0001.1, 2017.

Luke, E. P. and Kollias, P.: Separating Cloud and Drizzle Radar Moments during Precipitation Onset Using Doppler Spectra, Journal of Atmospheric and Oceanic Technology, 30, 1656–1671, https://doi.org/10.1175/JTECH-D-11-00195.1, 2013.

Luke, E. P., Kollias, P., Johnson, K. L., and Clothiaux, E. E.: A Technique for the Automatic Detection of Insect Clutter in Cloud Radar Returns, Journal of Atmospheric and Oceanic Technology, 25, 1498–1513, https://doi.org/10.1175/2007JTECHA953.1, 2008.

Luke, E. P., Kollias, P., and Shupe, M. D.: Detection of supercooled liquid in mixed-phase clouds using radar Doppler spectra, Journal of Geophysical Research, 115, https://doi.org/doi:10.1029/2009JD012884, 2010.

Maahn, M. and Löhnert, U.: Potential of Higher-Order Moments and Slopes of the Radar Doppler Spectrum for Retrieving Microphysical and Kinematic Properties of Arctic Ice Clouds, Journal of Applied Meteorology and Climatology, 56, 263–282, https://doi.org/10.1175/JAMC-D-16-0020.1, 2017.

Matrosov, S. Y. and Kropfli, R. A.: Cirrus Cloud Studies with Elliptically Polarized Ka-band Radar Signals: A Suggested Approach, Journal of Atmospheric and Oceanic Technology, 10, 684–692, https://doi.org/10.1175/1520-0426(1993)010<0684:CCSWEP>2.0.CO;2, 1993.

Myagkov, A., Seifert, P., Wandinger, U., Bauer-Pfundstein, M., and Matrosov, S. Y.: Effects of Antenna Patterns on Cloud Radar Polarimetric Measurements, Journal of Atmospheric and Oceanic Technology, 32, 1813–1828, https://doi.org/10.1175/JTECH-D-15-0045.1, 2015.

Myagkov, A., Seifert, P., Wandinger, U., Bühl, J., and Engelmann, R.: Relationship between temperature and apparent shape of pristine ice crystals derived from polarimetric cloud radar observations during the ACCEPT campaign, Atmospheric Measurement Techniques, 9, 3739–3754, https://doi.org/10.5194/amt-9-3739-2016, 2016.

Oue, M., Kollias, P., Ryzhkov, A., and Luke, E. P.: Toward Exploring the Synergy Between Cloud Radar Polarimetry and Doppler Spectral Analysis in Deep Cold Precipitating Systems in the Arctic, Journal of Geophysical Research: Atmospheres, 123, 2797–2815, https://doi.org/10.1002/2017JD027717, 2018.

Petäjä, T., O'Connor, E. J., Moisseev, D., Sinclair, V. A., Manninen, A. J., Väänänen, R., von Lerber, A., Thornton, J. A., Nicoll, K., Petersen, W., Chandrasekar, V., Smith, J. N., Winkler, P. M., Krüger, O., Hakola, H., Timonen, H., Brus, D., Laurila, T., Asmi, E., Riekkola, M.-L., Mona, L., Massoli, P., Engelmann, R., Komppula, M., Wang, J., Kuang, C., Bäck, J., Virtanen, A., Levula, J., Ritsche, M., and Hickmon, N.: BAECC: A Field Campaign to Elucidate the Impact of Biogenic Aerosols on Clouds and Climate, Bulletin of the American Meteorological Society, 97, 1909–1928, https://doi.org/10.1175/BAMS-D-14-00199.1, 2016.

Pfitzenmaier, L., Dufournet, Y., Unal, C. M. H., and Russchenberg, H. W. J.: Retrieving Fall Streaks within Cloud Systems Using Doppler Radar, Journal of Atmospheric and Oceanic Technology, 34, 905–920, https://doi.org/10.1175/JTECH-D-16-0117.1, 2017.

Radenz, M., Bühl, J., Lehmann, V., Görsdorf, U., and Leinweber, R.: Combining cloud radar and radar wind profiler for a value added estimate of vertical air motion and particle terminal velocity within clouds, Atmospheric Measurement Techniques, 11, 5925–5940, https://doi.org/10.5194/amt-11-5925-2018, 2018.

Radenz, M., Bühl, J., and Seifert, P.: peakTree version of Feb2019, https://doi.org/10.5281/zenodo.2577387, 2019.

Rambukkange, M. P., Verlinde, J., Eloranta, E. W., Flynn, C. J., and Clothiaux, E. E.: Using Doppler Spectra to Separate Hydrometeor Populations and Analyze Ice Precipitation in Multilayered Mixed-Phase Clouds, IEEE Geoscience and Remote Sensing Letters, 8, 108–112, https://doi.org/10.1109/LGRS.2010.2052781, 2011.

Rose, T., Crewell, S., Löhnert, U., and Simmer, C.: A network suitable microwave radiometer for operational monitoring of the cloudy atmosphere, Atmospheric Research, 75, 183–200, 2005.

Schmithüsen, H.: Upper air soundings during POLARSTERN cruise PS106.2 (ARK-XXXI/1.2), https://doi.org/10.1594/PANGAEA.882843, 2017.

Shupe, M. D., Uttal, T., Matrosov, S. Y., and Frisch, A. S.: Cloud water contents and hydrometeor sizes during the FIRE Arctic Clouds Experiment, Journal of Geophysical Research: Atmospheres, 106, 15 015–15 028, https://doi.org/10.1029/2000JD900476, 2001.

Shupe, M. D., Kollias, P., Matrosov, S. Y., and Schneider, T. L.: Deriving Mixed-Phase Cloud Properties from Doppler Radar Spectra, Journal of Atmospheric and Oceanic Technology, 21, 660–670, https://doi.org/10.1175/1520-0426(2004)021<0660:DMCPFD>2.0.CO;2, 2004.

Shupe, M. D., Comstock, J. M., Turner, D. D., and Mace, G. G.: Cloud Property Retrievals in the ARM Program, Meteorological Monographs, 57, 19.1–19.20, https://doi.org/10.1175/AMSMONOGRAPHS-D-15-0030.1, 2016.

Verlinde, J., Rambukkange, M. P., Clothiaux, E. E., McFarquhar, G. M., and Eloranta, E. W.: Arctic multilayered, mixed-phase cloud processes revealed in millimeter-wave cloud radar Doppler spectra, Journal of Geophysical Research: Atmospheres, 118, 199–213, https://doi.org/10.1002/2013JD020183, 2013.

Wakasugi, K., Mizutano, M., Matsuo, M., Fukao, S., and Kato, S.: A direct method of deriving drop size distribution and vertical air velocities from VHF Doppler radar spectra, Journal of Atmospheric and Oceanic Technology, 3, 623–629, https://doi.org/10.1175/1520-0426(1986)003<0623:ADMFDD>2.0.CO;2, 1986.

Wang, Z. and Sassen, K.: Cirrus Cloud Microphysical Property Retrieval Using Lidar and Radar Measurements. Part I: Algorithm Description and Comparison with In Situ Data, Journal of Applied Meteorology, 41, 218–229, https://doi.org/10.1175/1520-0450(2002)041<0218:CCMPRU>2.0.CO;2, 2002.

Wang, Z., Sassen, K., Whiteman, D. N., and Demoz, B. B.: Studying Altocumulus with Ice Virga Using Ground-Based Active and Passive Remote Sensors, Journal of Applied Meteorology, 43, 449–460, https://doi.org/10.1175/1520-0450(2004)043<0449:SAWIVU>2.0.CO;2, 2004.

Wendisch, M., Macke, A., Ehrlich, A., Lüpkes, C., Mech, M., Chechin, D., Dethloff, K., Barientos, C., Bozem, H., Brückner, M., Clemen, H.-C., Crewell, S., Donth, T., Dupuy, R., Ebell, K., Egerer, U., Engelmann, R., Engler, C., Eppers, O., Gehrmann, M., Gong, X., Gottschalk, M., Gourbeyre, C., Griesche, H., Hartmann, J., Hartmann, M., Heinold, B., Herber, A., Herrmann, H., Heygster, G., Hoor, P., Jafariserajehlou, S., Jäkel, E., Järvinen, E., Jourdan, O., Kästner, U., Kecorius, S., Knudsen, E. M., Köllner, F., Kretzschmar, J., Lelli, L., Leroy, D., Maturilli, M., Mei, L., Mertes, S., Mioche, G., Neuber, R., Nicolaus, M., Nomokonova, T., Notholt, J., Palm, M., van Pinxteren, M., Quaas, J., Richter, P., Ruiz-Donoso, E., Schäfer, M., Schmieder, K., Schnaiter, M., Schneider, J., Schwarzenböck, A., Seifert, P., Shupe, M. D., Siebert, H., Spreen, G., Stapf, J., Stratmann, F., Vogl, T., Welti, A., Wex, H., Wiedensohler, A., Zanatta, M., and Zeppenfeld, S.: The Arctic Cloud Puzzle: Using ACLOUD/PASCAL Multi-Platform Observations to Unravel the Role of Clouds and Aerosol Particles in Arctic Amplification, Bulletin of the American Meteorological Society, 100, 841–871, https://doi.org/10.1175/BAMS-D-18-0072.1, 2019.

Williams, C. R., Maahn, M., Hardin, J. C., and de Boer, G.: Clutter mitigation, multiple peaks, and high-order spectral moments in 35 GHz vertically pointing radar velocity spectra, Atmospheric Measurement Techniques, 11, 4963–4980, https://doi.org/10.5194/amt-11-4963-2018, 2018.

Yu, G., Verlinde, J., Clothiaux, E. E., and Chen, Y.-S.: Mixed-phase cloud phase partitioning using millimeter wavelength cloud radar Doppler velocity spectra, Journal of Geophysical Research: Atmospheres, 119, 7556–7576, https://doi.org/10.1002/2013JD021182, 2014.

Zhao, C., Xie, S., Klein, S. A., Protat, A., Shupe, M. D., McFarlane, S. A., Comstock, J. M., Delanoë, J., Deng, M., Dunn, M., Hogan, R. J., Huang, D., Jensen, M. P., Mace, G. G., McCoy, R., O'Connor, E. J., Turner, D. D., and Wang, Z.: Toward understanding of differences in current cloud retrievals of ARM ground-based measurements, Journal of Geophysical Research: Atmospheres, 117, https://doi.org/10.1029/2011JD016792, 2012.